PROBING THE SUPERCONDUCTING PROXIMITY EFFECT IN TOPOLOGICAL INSULATORS

By

Matthias Muenks

A THESIS

Submitted to
Michigan State University
in partial fulfillment of the requirements
for the degree of

Physics - Master of Science

2013

ABSTRACT
PROBING THE SUPERCONDUCTING PROXIMITY EFFECT IN TOPOLOGICAL INSULATORS

By

Matthias Muenks

Topological Insulators have been a major focus in condensed-matter physics over the past six years. It was realized that the spin polarized surface states of topological insulators can lead to novel applications in spintronics or even in quantum computing. The exciting physics includes the famous Majorana fermion, believed to arise when a topological insulator is brought in close proximity to a s-wave superconductor, resulting in an artificial p-wave like superconductor. This thesis contributes to this ongoing research by describing the underlying theory and investigating the necessary steps to create a successful interface between a topological insulator and a s-wave superconductor, thus laying the groundwork for probing the proximity effect in these interfaces with Scanning Tunneling Spectroscopy. Nb, Pb and PbBi structures were investigated and a suitable geometry, that was grown with a shadow mask, is presented.

TABLE OF CONTENTS

LIST OF FIGURES

Chapter 1

Introduction

The discovery of the Integer Quantum Hall State in 1980 [17] led to a novel approach in band theory that utilizes topological arguments that are directly related to the geometry of the Brillouin zone [2] [32] [5] [6]. This deep connection between geometry, topology and band theory will be shown in the first chapter which introduces the theory of topological insulators. A famous application of topological band theory is the prediction of the Quantum Spin Hall State; moreover, topological insulator behavior has been verified by Scanning Tunneling Spectroscopy and Angle Resolved Photoemission Spectroscopy [13] [26] [27]. The theoretical prediction of the emergence of Majorana fermions in a p-wave superconductor has been known for almost over a decade [16] but since no verified and suitable p-wave superconductor was initially available, only a few experiments that created a fake p-wave superconductor were available to the scientific community [23]. A novel approach that involves topological insulators was suggested in 2007 by Fu and Kane [11] where they proposed to deposit a s-wave superconductor on a 3D topological insulator in order to create a 2D p-wave superconductor via the proximity effect. This thesis is organized as follows: Chapter 2 introduces the theory of topological insulators in terms of the Berry phase and Berry connection, describes the mentioned approach by Fu and Kane in detail, discusses Scanning Tunneling Microscopy and Spectroscopy, and proposes a Scanning Tunneling Spectroscopy experiment to probe the proximity effect. Before we can probe the proximity effect we must fabricate a suitable sample with a clean interface between a superconducting island and a topological insu-

lator. The available experimental techniques, sputtering of Nb and evaporation of Pb and PbBi, will be described in Chapter 3. The results will be presented in Chapter 4 and finally discussed in Chapter 5.

Chapter 2

Theory

This chapter describes very elegant ideas and principles that led to topological band theory. The Berry phase, Berry connection, and the first Chern number or Z invariant will be introduced with a review of the Integer Quantum Hall State that will lead to a similar approach in the Quantum Spin Hall State. The definition of topological insulators in terms of the Chern invariant or Z_2 invariant will be motivated. Majorana Fermions and p-wave superconductors are also briefly discussed. Less theoretically inclined readers may consider reading the introductory paragraph to section 2.1 and then skipping forward to section 2.2 where Scanning Tunneling Microscopy and Spectroscopy as well as its application and the thesis experiment are introduced.

2.1 Topological Insulators

In the past eight years, topological insulators have been among the hottest topics in condensed matter physics, with a wide variety of new applications such as Majorana fermions in quantum computing and even spintronics [13] [26] [27].

Phase transitions have been described with symmetry breaking in the Ginzburg-Landau framework, e.g., superconductivity, ferromagnets and charge density waves. All of them have a local order parameter in common. Recently there has been a discovery of new phase transitions that can not be described by a local order parameter but only by a nonlocal order parameter in the

framework of topological order. Band theory in condensed matter has now been extended into topological band theory with the Chern number and the Berry phase being among the most important new assets [Avron1983]. It is instructional to elaborate on the origin of these new concepts that will help to understand the framework of topological insulators and topological superconductors. The Integer Quantum Hall State, completely described with topological arguments, is a good starting point for this endeavor. The Integer Quantum Hall Effect can be extended into the Quantum Spin Hall State for which a similar topological obstruction can be made by invoking time reversal symmetry. These ideas formed the framework for the new classification of topological classes and a rigorous definition of topological insulators.

2.1.1 The notion of topology

Topology is the underlying keyword to describe most of the theory framework used for topological insulators. Shortly after the discovery of the Integer Quantum Hall Effect, Thouless et al. found a topological invariant that has been hiding in the Berry connection which is explicitly in the equation for the Hall conductance [34]. Charles Kane and Eugene Mele generalized these topological arguments for the Quantum Spin Hall Effect and for their classification of topological insulators involving topological invariants. It is therefore crucial to shine some light on the basics of topology first.

Bob Franzosa from the University of Maine made a beautiful argument introducing topology by using the Koenigsberg bridges [1]. The Koenigsberg bridge problem is indeed a fascinating topic by itself and will be explained in detail on the following pages. In topology, absolute measures such as distance are not important but relative positions and arrangements are. A famous example consistently used in almost every introduction to topological insulators is the topological equivalence of a doughnut and a coffee cup, which can be deformed into each other as long as they are not torn. But how is a physicist supposed to use this information if we can't even tell the difference between a doughnut and a coffee cup? It is helpful to start by realizing that topological arguments are a qualitative tool that allows us to

- identify possibilities or impossibilities
- confirm existence or nonexistence.

In the year 1736 when Leonhard Euler was residing in Koenigsberg, back then part of Prussia and full of bridges, he asked himself if there is a way to cross all bridges without crossing a bridge twice, see figure 2.1. Basically a simple question which can only have one answer: yes or no. Euler found a solution to this problem and published his results in a paper with the translated title:

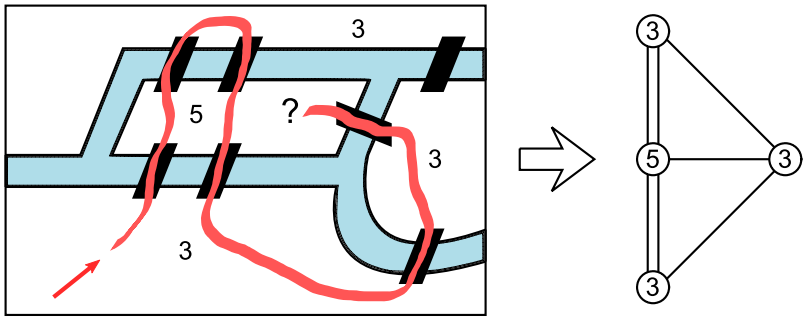

Figure 2.1: Left: The Seven Bridges of Koenigsberg represented by four landmasses (white) separated by a river with two branches (blue) and seven bridges (black). A possible path (red) which starts at the bottom left and leads to a dead end before every bridge was visited is shown. Right: Simplifying the connection information content of this arrangement with graph theory where every landmass is now represented by an abstract vertex and every bridge by an edge. The numbers define the number of edges for each vertex. *For interpretation of the references to color in this and all other figures, the reader is referred to the electronic version of this thesis.*

"The solution of a problem relating to the geometry of position". The term "geometry of position" already suggests that he was dealing with something new. Euler found that the solution does not depend on the total number of edges but on the number of edges for each vertex. He showed that for an odd number of edges for each vertex there is no solution meaning we cannot cross every bridge only once and still visit every landmass, we will therefore end up with two dangling ends of our path that can never be connected as displayed in figure 2.1. For an even number of edges for each vertex there is always one solution and the starting point and ending point are the same which leads to a closed loop. In the case where there are two even and two odd numbers coexisting we see that we indeed have a solution, meaning we can cross every bridge just once and visit every landmass, but we will not end up at the same point and again we end up with two dangling ends of our path that can not be connected to a closed loop. Interestingly the starting point will then be in a vertex with an odd number of connections and the ending point will the in the other vertex with an odd number of connections. If more than two vertices have an odd number of connections,

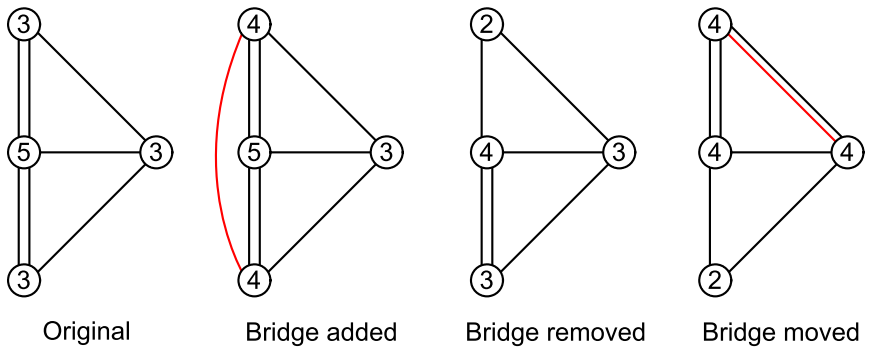

Figure 2.2: An example of modifying the edges. To change the number of edges, three modifications to the original arrangement have been made: One edge was added, one edge was removed and one edge was simply moved to another vertex. Notice that all edges for each vertex in the original arrangement are odd (3/5/3/3) while for the last case they are all even (4/4/2/4).

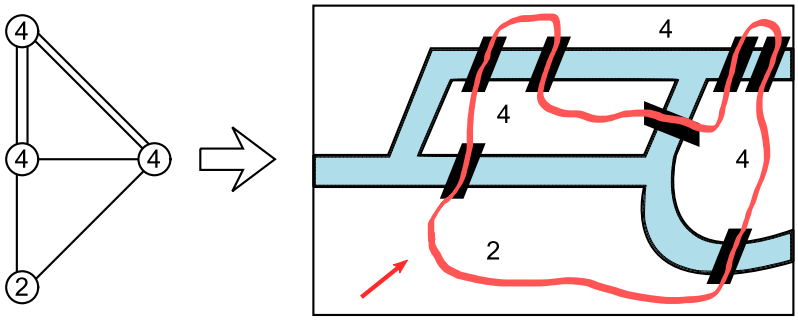

Figure 2.3: Left: The graph of the last modification from figure 2.8 where all vertices have an even number of edges. Right: Visualizing the meaning of a closed path by transforming the information contained in vertices and edges back to landmasses and bridges.

then there will be no solution. In summary, we can focus on the two cases with only even or odd connections to capitalize the importance of parity (in a mathematical sense):

- All edges are **odd**: No solution. Path has two dangling ends that are stuck in two different vertices.
- All edges are **even**: Existence of one path that covers all edges and ends in the same vertex where it started.

This reasoning can be used in physics as well. In condensed matter, we first need to specify the space in which we are using topological arguments. It is not real space in which Euler was reasoning about crossing bridges. In condensed matter the wavefunctions in a periodic crystal are described by a Hamiltonian $H(\mathbf{k})$ that can be diagonalized to find its eigenvalues $E(\mathbf{k})$ which define energy bands and therefore the entire bandstructure of the system. Now, the momentum $\mathbf{k}$ lives in momentum space and $H(\mathbf{k})$ in Hilbert space. It is a complication that we do not have only one space to consider like Euler, but we have two spaces: Hilbert space and momentum space. An abstract but complete description relates the topology of two spaces to each other using the theory of fiber bundles, but this approach would be too ambitious for an introduction. We will rather focus on the Berry connection that was basically invented for physicists that do not want to bother with the theory of fiber bundles and nontrivial holonomy groups. In a naive way the bridges are the energy eigenstates of the Hamiltonian, the landmasses represent a part of the momentum space, or better a part of the Hilbert space that is a function of momentum in momentum space, and the river is the Fermi energy. To gain a better understanding of the Berry connection we will take a closer look at the Integer Quantum Hall Effect.

A Hamiltonian that depends on any additional parameters can have a Berry phase that is calculated via the Berry connection [5] [2]. In band theory, the Bloch Hamiltonian H generally depends on the crystal momentum $\mathbf{k}$ and the eigenstates of the Bloch Hamiltonian are Bloch wavefunctions which are defined in a periodic unit cell:

$$H(\mathbf{k})\,|u(\mathbf{k})\rangle = E(\mathbf{k})\,|u(\mathbf{k})\rangle\,. \tag{2.1}$$

Based on this, the Berry connection[1] is defined as:

$$\mathbf{A}(\mathbf{k}) = -i \langle u(\mathbf{k}) | \nabla_{\mathbf{k}} | u(\mathbf{k}) \rangle . \tag{2.2}$$

Based on this definition, we now see that a gauge transformation on the wavefunctions

$$|u'(\mathbf{k})\rangle \to e^{i\chi(\mathbf{k})} |u(\mathbf{k})\rangle \tag{2.3}$$

will lead to an additional gradient of this phase in the Berry connection:

$$\begin{aligned} \mathbf{A}'(\mathbf{k}) &= -i \langle u(\mathbf{k}) e^{-i\chi(\mathbf{k})} | \nabla_{\mathbf{k}} e^{i\chi(\mathbf{k})} | u(\mathbf{k}) \rangle & (2.4) \\ &= -i \left(\langle u(\mathbf{k}) | \nabla_{\mathbf{k}} | u(\mathbf{k}) \rangle + i \nabla_{\mathbf{k}} \chi(\mathbf{k}) \right) & (2.5) \\ &= \mathbf{A}(\mathbf{k}) + \nabla_{\mathbf{k}} \chi(\mathbf{k}). & (2.6) \end{aligned}$$

The Berry phase γ arises due to the integration of the Berry connection on a closed loop in momentum space:

$$\gamma = \oint d\mathbf{k} \cdot \mathbf{A}(\mathbf{k}) = i \oint d\mathbf{k} \cdot \left(\langle u(\mathbf{k}) | \nabla_{\mathbf{k}} | u(\mathbf{k}) \rangle \right) . \tag{2.7}$$

By using Stokes' theorem, the closed line integral can be rewritten as the surface integral over the rotation of the Berry connection:

$$\gamma = \oint d\mathbf{k} \cdot \mathbf{A}(\mathbf{k}) = \iint d\mathbf{k} \nabla \times \mathbf{A}(\mathbf{k}) \tag{2.8}$$

[1] The interested reader might wonder where this definition comes from. From a mathematical point of view one has to learn more about fiber bundles. From a physical point of view, the Integer Quantum Hall Effect that is described in the next section will give a better understanding since a real physical quantity, the conductance, explicitly contains the Berry connection, that is basically just a tool to measure the curvature of momentum space and relates the space's geometry to its topology.

where a few people simplify this further by introducting the Berry flux $\iint d\mathbf{k}F(\mathbf{k})$ or the Berry curvature $\Omega = \nabla \times A$.

2.1.2 Integer Quantum Hall State

Hall's measurements back in 1879 showed that the Hall voltage is linearly dependent on the applied current and the magnetic field. A surprising turn of events came in 1980 when von Klitzling discovered a striking new behaviour of this voltage [17]. He discovered that it is in fact quantized. He identified a quantization that is proportional to the Hall conductivity σ:

$$\sigma = n\frac{e^2}{h} \tag{2.9}$$

where e is the charge of the electron, h is Planck's constant and n is an integer. The term e^2/h in equation 2.9 is a fundamental constant of nature. Von Klitzing showed that the term e^2/h can be evaluated very precisely and was awarded the 1985 Nobel Prize in Physics for this discovery in 1980. The inverse of this term is called the von Klitzing constant $R_{\mathrm{K}} = h/e^2 = 25812.8074434(84)\Omega$ which defines a resistance and has been identified in one part of a billion, regardless of imperfections of the sample or the geometric details of the experiment. One year later, Laughlin argued that this precise quantization must be due to an underlying general principle [21]. Again, one year later in 1982, Thouless, Kohmoto, Nightingale and den Nijs (TKNN) showed that this general principle is related to the geometry of momentum space [34]. Physicists, first unaware of the deep topological connection, described the integer n in equation 2.9 as the so called TKNN-invariant, later shown to be the first Chern number in the mathematical language that was developed long before. In a follow-up paper from 1984 [18], Kohmoto made it very clear how geometry and topology are related to the IQHE based on the insights in 1984 from Sir Berry who introduced the Berry connection and the Berry phase [5] and Avron who worked on a new topological band theory [2]. I will follow the language and understanding of Mahito Kohmoto as described in his follow up-paper for [34] from 1985 [18].

As the angular momentum is the generator of rotation, the momentum is the generator of translation:

$$\hat{T} = e^{\frac{i}{\hbar}\mathbf{r}\cdot\mathbf{p}}. \tag{2.10}$$

In general, the Hamiltonian of an electron in a periodic potential $V(\mathbf{r})$

$$H = \frac{1}{2m}\mathbf{p}^2 + V(\mathbf{r}) \tag{2.11}$$

does commute with this translation operator $[H, \hat{T}] = 0$ for a discrete number of lattice spacings and is thus invariant under the translation group. Therefore we can define Bloch states which have this periodicity in the form of their energy eigenfunctions that is the product of a plane wave and a periodic Bloch function:

$$\psi_{n\mathbf{k}}(\mathbf{r}) = e^{i\mathbf{k}\cdot\mathbf{r}} u_{n\mathbf{k}}(\mathbf{r}), \tag{2.12}$$

where $\mathbf{k}$ is the wave vector and the index n labels the energy bands. What if we also apply a constant magnetic field to the electron in a periodic potential? The Hamiltonian

$$H = \frac{1}{2m}(\mathbf{p} + e\mathbf{A})^2 + V(\mathbf{r}) \tag{2.13}$$

is no longer invariant under the translation group and we're forced to define new translation operators, the so called *magnetic translation operators*. We need to reverse the effect on the momentum of the applied magnetic field, since $\mathbf{p} \to \mathbf{p} + e\mathbf{A}$ and we can now define new magnetic translation operators that will commute with the Hamiltonian:

$$\hat{T} = e^{\frac{i}{\hbar}\mathbf{R}\cdot(\mathbf{p} - e\mathbf{A})} \tag{2.14}$$

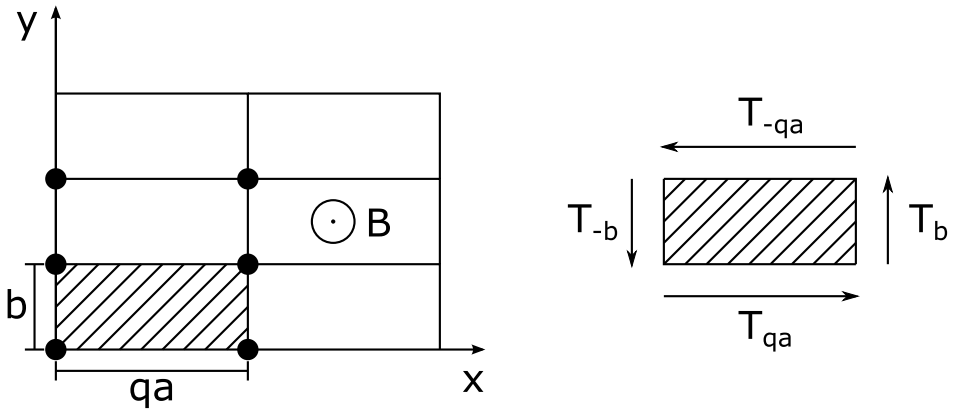

Figure 2.4: Enlarged Magnetic unit cell in a periodic lattice. The magnetic field **B** is perpendicular to the *xy*-plane. The four magnetic translation operators describe a closed path around one enlarged magnetic unit cell on the right.

which indeed commute with the Hamiltonian $[\hat{T},H]=0$ if we choose a symmetric gauge

$$\mathbf{A}=\frac{1}{2}(\mathbf{r}\times\mathbf{B}). \tag{2.15}$$

Having taken care of new translation operators, we can now define new Bloch functions for a periodic potential $U(x+a,y)=U(x,y+b)=U(x,y)$ and a Bravais lattic vector:

$$\mathbf{R}=n\mathbf{a}+m\mathbf{b} \tag{2.16}$$

that is used as a shift in our translation operators ($\hat{T}f(\mathbf{r})=f(\mathbf{r}+\mathbf{R})$). These magnetic translation operators do not commute with each other and we get a phase

$$\hat{T}_a\hat{T}_b=e^{2\pi i\Phi}\hat{T}_a\hat{T}_b, \tag{2.17}$$

where Φ is the number of magnetic flux quanta in one unit cell (a,b). The magnetic translation

operators only commute with each other if the phase is equal to one $e^{2\pi i\Phi} = 1$. This is only true if Φ is an integer. In order to get a meaningful number of flux quanta greater than zero we define an enlarged unit cell

$$\mathbf{R} = n(q\mathbf{a}) + m\mathbf{b}. \tag{2.18}$$

By enlarging the unit cell by q we simultaneously decrease the Brillouin zone in reciprocal space by q, which we will call the magnetic Brillouin zone (MBZ) from now on. Eigenfunctions and eigenvalues are a function of momenta $\left(0 \leq k_x \leq \frac{2\pi}{qa}\right)$ and $\left(0 \leq k_y \leq \frac{2\pi}{b}\right)$ as:

$$\hat{T}_{qa}\psi = e^{ik_x qa}\psi \tag{2.19}$$

$$\hat{T}_b\psi = e^{ik_y b}\psi. \tag{2.20}$$

According to Bloch's theorem we can now define periodic eigenfunctions:

$$\Psi^{\alpha}_{k_x k_y}(x,y) = e^{ik_x x + ik_y y} u^{\alpha}_{k_x k_y}(x,y), \tag{2.21}$$

where α is the band index. Under translation, we now get

$$u^{\alpha}_{k_x k_y}(x+qa,y) = e^{-i\pi py/b} u^{\alpha}_{k_x k_y}(x,y) \tag{2.22}$$

$$u^{\alpha}_{k_x k_y}(x,y+b) = e^{i\pi px/qa} u^{\alpha}_{k_x k_y}(x,y) \tag{2.23}$$

When we now go around the boundary of our unit cell $(x,y) \to (x+qa,y) \to (x+qa,y+b) \to (x,y+b) \to (x,y)$ which is equal to applying four magnetic translation operators $\hat{T}_{qa}\hat{T}_b\hat{T}_{-qa}\hat{T}_{-b} =$

1, we get an explicit expression for the phase change:

$$\hat{T}_{qa}\hat{T}_b\hat{T}_{-qa}\hat{T}_{-b} = e^{2\pi i\frac{eB}{h}aqb} = 1. \tag{2.24}$$

This statement is only true if:

$$\frac{eB}{h}aqb = p. \tag{2.25}$$

where p is an integer. This is directly proportional to the number of flux quanta which is fixed by the magnetic field going through the magnetic unit cell and cannot be changed by choosing a different vector potential $\mathbf{A}$. The number of flux quanta or the total vorticity is therefore a topological constraint. In an alternative way we can define that $u_{k_xk_y}(x,y) = |u_{k_xk_y}(x,y)|e^{i\theta_{k_xk_y}(x,y)}$ and get:

$$p = \frac{-1}{2\pi}\int d\vec{l}\cdot\frac{\partial\theta_{k_xk_y}(x,y)}{d\vec{l}}. \tag{2.26}$$

In a modern interpretation: $p = n$ = The first Chern number, which is expressed as the winding number of the Berry phase of electron wavefunctions around the Brillouin zone, but this will be more clear when we see the Berry connection in the conductance.

Let us explicitly add the periodic potential $U(x,y)$ of the crystal lattice to our Hamiltonian

$$\left(\frac{1}{2m}(\mathbf{p}+e\mathbf{A})^2 + U(x,y)\right)\psi = E\psi. \tag{2.27}$$

We can rewrite this Hamiltonian with Bloch functions $u^{\alpha}_{k_x k_y}$ which obey the periodic lattice:

$$H(k_x,k_y)u^{\alpha}_{k_x k_y} = E\alpha u^{\alpha}_{k_x k_y} \tag{2.28}$$

$$\left(\frac{1}{2m}(-i\hbar\nabla+\hbar\mathbf{k}+e\mathbf{A})^2+U(x,y)\right)u^{\alpha}_{k_x k_y} = E\alpha u^{\alpha}_{k_x k_y} \tag{2.29}$$

Now let's apply an electric field E_x in x-direction to our Hall sample. This can be seen as a small perturbation of an electric potential which creates a resulting current. We know that this potential is $U = \int F(x)dx = eE_x x$. If we treat x as an operator $x \to i\hbar\frac{\partial}{\partial p_x}$ and use $\partial p_x = \hbar\partial k_x$ we get for our applied potential

$$U = ieE_x\frac{\partial}{\partial k_x}. \tag{2.30}$$

For a more thorough treatment we could use a linear respone function, the Kubo formula, which allows a change in temperature and a many body treatment in form of Green's functions. According to Laughlin's argument, the number and nature of the current-carrying state is irrelevant [21]. For the sake of simplicity we can gain a first understanding by just considering one electron at 0 Kelvin. Now we use the general time-independent perturbation as shown in equation 2.31 and keep only terms with $\lambda = 1$ for a first order perturbation of our unperturbed state $|u^{\alpha}\rangle$.

$$|n\rangle^{(\lambda)} = |n\rangle^{(0)} + \lambda\sum_{k\neq n}\frac{|k\rangle^{(0)}\langle k|^{(0)}U|n\rangle^{(0)}}{E_n^{(0)}-E_k^{(0)}} \tag{2.31}$$

$$\to |u^{\alpha}\rangle^{(1)} = |u^{\alpha}\rangle + ieE_x\sum_{\beta\neq\alpha}\frac{|u^{\beta}\rangle\langle u^{\beta}|\frac{\partial}{\partial k_x}|n^{\alpha}\rangle}{E^{\alpha}-E^{\beta}}. \tag{2.32}$$

The electric potential in combination with the magnetic field will accelerate the electron and lead to an observable Hall current in y-direction. Hence we try to solve for the average velocity of the

electron in y-direction

$$v_y = \langle u^\alpha |^{(1)} \, v_y \, | u^\alpha \rangle^{(1)} \tag{2.33}$$

leading to

$$v_y = \langle u^\alpha | \, v_y \, | u^\alpha \rangle + ieE_x \sum_{\beta \neq \alpha} \frac{\langle u^\alpha | \, v_y \, | u^\beta \rangle \, \langle u^\beta | \, \frac{\partial}{\partial k_x} \, | u^\alpha \rangle}{E^\alpha - E^\beta} + \text{h.c.} \tag{2.34}$$

where h.c. stands for hermitian conjugate that will be left out in the following calculations for simpflication. In the Heisenberg picture we can express the operator $v_y = \frac{d}{dt} y$ as

$$\frac{d}{dt} y = \frac{i}{\hbar} [H, y]. \tag{2.35}$$

Using this expression we can write

$$\begin{aligned}
\langle u^\alpha | \, v_y \, | u^\beta \rangle &= \frac{i}{\hbar} \langle u^\alpha | \, [H, y] \, | u^\beta \rangle && (2.36)\\
&= \frac{i}{\hbar} \left(\langle u^\alpha | \, Hy \, | u^\beta \rangle - \langle u^\alpha | \, yH \, | u^\beta \rangle \right) && (2.37)\\
&= \frac{i}{\hbar} \langle u^\alpha | \, y \, | u^\beta \rangle \left(E^\alpha - E^\beta \right) && (2.38)\\
&= -\frac{1}{\hbar} \langle u^\alpha | \, \frac{\partial}{\partial k_y} \, | u^\beta \rangle \left(E^\alpha - E^\beta \right) && (2.39)
\end{aligned}$$

where we once again used $y \to i\hbar \frac{\partial}{\partial py} = i \frac{\partial}{\partial ky}$ in the last line. So we can rewrite our first expression for the average velocity as

$$v_y = \langle u^\alpha | \, v_y \, | u^\alpha \rangle - \frac{ieE_x}{\hbar} \left(\sum_{\beta \neq \alpha} \langle \frac{\partial u^\alpha}{\partial k_y} | u^\beta \rangle \, \langle u^\beta | \frac{\partial u^\alpha}{\partial k_x} \rangle \right). \tag{2.40}$$

Executing the sum over all bands β with the completeness relation $\sum_{\beta} |\beta\rangle \langle\beta| = 1$ yields

$$v_y = \langle u^\alpha | \, v_y \, | u^\alpha \rangle - \frac{ieE_x}{\hbar} \left(\langle \frac{\partial u^\alpha}{\partial k_x} | \frac{\partial u^\alpha}{\partial k_y} \rangle - \langle \frac{\partial u^\alpha}{\partial k_y} | \frac{\partial u^\alpha}{\partial k_x} \rangle \right). \tag{2.41}$$

The first term on the right hand side of equation 2.41 produces no current since an electron that moves from a band α to the same band α does not contribute. To find the actual Hall current in y-direction we integrate over all possible $\mathbf{k}$ values in the magnetic Brillouin zone (MBZ) for all average velocities:

$$\begin{aligned}
j_y &= -e \, n \, v && (2.42)\\
j_y &= -e \iint_{MBZ} \frac{dk_x dk_y}{(2\pi)^2} \sum_{\alpha} v_y^\alpha && (2.43)\\
&= \frac{E_x e^2}{h} \underbrace{\iint_{MBZ} \frac{dk_x dk_y}{(2\pi) i} \sum_{\alpha} \left(\langle \frac{\partial u^\alpha}{\partial k_y} | \frac{\partial u^\alpha}{\partial k_x} \rangle - \langle \frac{\partial u^\alpha}{\partial k_x} | \frac{\partial u^\alpha}{\partial k_y} \rangle \right)}_{\text{Chern number } n} && (2.44)\\
&= E_x \frac{e^2}{h} n && (2.45)\\
&= \sigma_{yx} E_x. && (2.46)
\end{aligned}$$

Comparing this form with equation 2.9 we see that n is indeed the Chern number. To see how this expression is related to the Berry connection, let us define a vector field in the magnetic Brillouin zone

$$\hat{\mathbf{A}}(k_x, k_y) = \langle u_{k_x k_y} | \, \nabla_k \, | u_{k_x k_y} \rangle \text{ with } \nabla_k = \begin{pmatrix} \frac{\partial}{\partial k_x} \\ \frac{\partial}{\partial k_y} \end{pmatrix}. \tag{2.47}$$

This vector field is just a tool that measures the curvature in our magnetic Brillouin zone by adding a geometric structure (basically just by taking the derivates with respect to k_x and k_y) and distin-

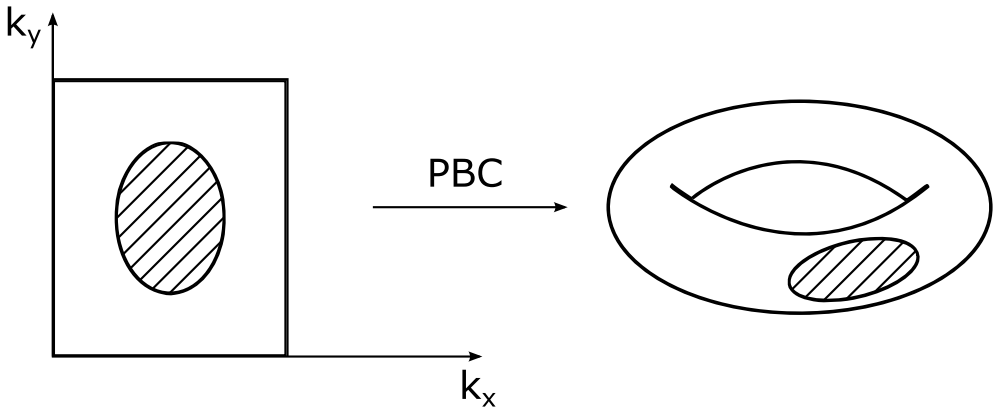

Figure 2.5: Magnetic Brillouin Zone and its representation as a torus when periodic boundary conditions (PBC) are applied. The torus is divided into two regions, where the shaded region contains a zero of the wavefunction.

guishes between different points in the Brillouin zone which map to different Hilbert spaces. If we assume periodic boundary conditions for our magnetic Brillouin zone, we see that we indeed get a curvature by having a torus. We now see that we can write the Chern number as the integral over the third component of a vector product:

$$\sigma_{xy}^{\alpha} = \frac{e^2}{h}\frac{1}{2\pi i}\iint\limits_{MBZ} dk_x dk_y [\nabla_k \times \hat{\mathbf{A}}(k_x,k_y)]_3. \tag{2.48}$$

This surface integral over the the curl of a vector field looks familiar, and indeed we can rewrite this expression by using Stokes' theorem:

$$\sigma_{xy}^{\alpha} = \frac{e^2}{h}\frac{1}{2\pi i}\iint\limits_{MBZ} dk_x dk_y [\nabla_k \times \hat{\mathbf{A}}(k_x,k_y)]_3 = \frac{e^2}{h}\frac{1}{2\pi i}\underbrace{\oint\limits_{\partial MBZ} \mathbf{A}(k_x,k_y)\cdot d\mathbf{k}}_{\text{Berry phase}}. \tag{2.49}$$

which is now precisely equal to the Berry phase that was defined earlier. We see that we get a line integral around the boundary of the MBZ. But since the MBZ has periodic boundary condi-

tions, we do not have a boundary and Stokes theorem gives us zero which would also be true for integrating the Gaussian curvature of a torus. Moreover, since the global topology of this space is non-contractible, i.e. it cannot be continuously shrunk to a point, we still get a topological invariant upon integration. This topological feature is in fact closely related to a gauge transformation. We could fix the gauge by demanding a real amplitude $\langle a|u(\mathbf{k})\rangle$ where $\langle a|$ is an arbitrary wavefunction, but this will not fix the gauge at the zeros of the amplitude. Near the zero we must therefore have another gauge and upon integration the phase mismatch between these two gauges produces a non-zero value of the line integral.

The location of the zeros does indeed depend on the gauge. As shown earlier, the total number of zeros is gauge invariant and is called the first Chern number of the principal U(1) bundle. Let's assume that we only have one point in the MBZ where $u^{\alpha}_{k_x k_y}(x,y)$ is zero. To account for the existing zero, we can split our MBZ into two regions, one of them containing the zero of the wavefunction, and see that we get a phase mismatch at the boundary of these two regions. This phase mismatch $|u^{II}_{k_x k_y}\rangle = e^{i\chi(k_x k_y)}\,|u^{I}_{k_x k_y}\rangle$ will manifest itself in the Berry connections $\mathbf{A}(k_x k_y)$ by a gauge transformation that will have no direct effect on the total conductance since the rotation of a gradient is always zero ($\nabla \times (\nabla f) = 0$):

$$\hat{\mathbf{A}}_{II}(k_x,k_y) = \hat{\mathbf{A}}_{I}(k_x,k_y) + i\nabla_k \chi(k_x k_y). \tag{2.50}$$

We can apply Stokes' theorem for region I and II:

$$\sigma_{xy} = \frac{e^2}{h}\frac{1}{2\pi i}\left(\iint_I dk_x dk_y [\nabla_k \times \hat{\mathbf{A}}_{\boldsymbol{I}}(k_x,k_y)]_3 + \iint_{II} dk_x dk_y [\nabla_k \times \hat{\mathbf{A}}_{\boldsymbol{II}}(k_x,k_y)]_3\right) \quad (2.51)$$

$$= \frac{e^2}{h}\frac{1}{2\pi i}\left(\oint_{\partial(I+II)} [\hat{\mathbf{A}}_{\boldsymbol{I}}(k_x,k_y) - \hat{\mathbf{A}}_{\boldsymbol{II}}(k_x,k_y)] \cdot d\mathbf{k}\right) \quad (2.52)$$

$$= \frac{e^2}{h}\underbrace{\frac{1}{2\pi}\oint_{\partial(I+II)} d\mathbf{k}\cdot\nabla_k \chi(k_x,k_y)}_{n} \quad (2.53)$$

$$= \frac{e^2}{h} n. \quad (2.54)$$

Here we have used the fact that a torus does not have a boundary and therefore region *I* and *II* must have opposite orientation which leads to the minus sign in equation 2.61. Since the state vectors have the same orientation at the starting and ending point of the integration, n is an integer and is equivalent to the winding number which we have found previously. The theory of fiber bundles can be used to generalize this argument to more than one zero.

The interested reader can read more about the Chern number and its relation to electromagnetism, where the Chern number can be seen as the total magnetic charge inside the MBZ (magnetic monopoles) in Chapter IV *(Fiber Bundle and Chern Class)* of Kohmoto's paper [18]. We have seen that the winding number, which is a topological constraint, is also present in the curvature of the magnetic Brillouin zone and can be expressed via the Berry connection and Berry phase. The number of zeros is equal to the number of magnetic flux quanta in the MBZ which is equal to the first Chern number (or Chern invariant Z), precisely equal to the number of edge states in the Integer Quantum Hall State. If the magnetic field is increased, the number of flux quanta per unit cell is increased as well as the conductance.

2.1.3 Quantum Spin Hall State

The IQHS needed an external magnetic field to show topologically protected edge states. Is there a way to get edge states without an external magnetic field? One approach would be to look for internal or intrinsic magnetic fields that are part of the system such as spin-orbit coupling. A system with edge states due to intrinsic spin-orbit coupling is called the Quantum Spin Hall State (QSHS). A first simple approach is to consider two copies of the IQHS with edge states that have different spin and are propagating in opposite directions. Here we can define two different Chern numbers (two different winding numbers, one positive, the other negative): $C_{\uparrow}$ for all edge states with spin up and momentum **k** and $C_{\downarrow}$ for all edge states with spin down and momentum **-k**. If spin is conserved then the sum of these two Chern numbers is zero: $C_{\uparrow} + C_{\downarrow} = 0$. The difference $C_{\uparrow} - C_{\downarrow}$ is not zero. If spin would be conserved, we could use this and define a new topological invariant, the so called Chern parity or Z_2 invariant ν.3,b,, , However, spin is normally not conserved in a real system and this approach is doomed to fail. In 2005, Kane and Mele realized that time-reversal symmetry is enough to define a Z_2 invariant ν, even when spin is not conserved [15]. I will follow the insights from Liang Fu, a renowned student from then Kane group (described in his thesis) from 2009 and detailed calculations from Bernevig and Hughes [4]. Time reversal symmetry is an important property especially when applied to fermions (half-integer spin) and bosons (integer spin). If the time reversal operator acts twice on a fermion, it rotates the spin by 2π. If it acts on a boson twice it is just the identity operator. The time reversal operator for fermions can be written as:

$$\Theta = e^{i\pi Sy} K \tag{2.55}$$

where K is the complex conjugation, S_y the half-integer spin and $\Theta^2 = -1$ as mentioned. Since the time reversal operator commutes with the Bloch Hamiltonian ($[H, \Theta] = 0$) we have:

$$H(-\mathbf{k}) = \Theta H(\mathbf{k})\Theta^{-1}. \tag{2.56}$$

Kramers' theorem [37] states, that if a fermionic system is subject only to an electric field as an allowed perturbation [2], then every energy eigenstate is at least doubly degenerate. If the system is subject to a magnetic field, the degeneracy splits up. In the case of spin orbit coupling, every eigenstate at **k** is degenerate with its time reversed partner at **-k**.

For the IQHE, we have seen that the Chern invariant can be defined by using Stokes' theorem and considering the right gauge. This is basically an obstruction to finding a smooth gauge for the Bloch wavefunctions due to the zeros of the wavefunctions that are caused by an external magnetic field. A similar obstruction can be found if we consider time reversal symmetry for the Bloch wavefunctions:

$$|u^I_\alpha(-\mathbf{k})\rangle \quad = \quad \Theta\,|u^{II}_\alpha(\mathbf{k})\rangle \tag{2.57}$$

$$\text{Multiplying } \Theta \quad \text{and} \quad (\Theta^2 = -1) \text{ gives:}$$

$$\Theta\,|u^I_\alpha(\mathbf{k})\rangle \quad = \quad -|u^{II}_\alpha(-\mathbf{k})\rangle \tag{2.58}$$

where I and II stand for the two Kramers' doublets and α goes from 1 to N for $2N$ wavefunctions in total. Now, instead of the Chern invariant Z, we can define a Chern parity or Z_2 invariant ν, where $\nu = 0$ describes a normal insulator and $\nu = 1$ a topological insulator. Let's assume that we have $2N$ occupied bands, where the 2 already explicitly stands for spin-up and spin-down

[2] Because an electric field does not destroy the time reversal symmetry of the Hamiltonian.

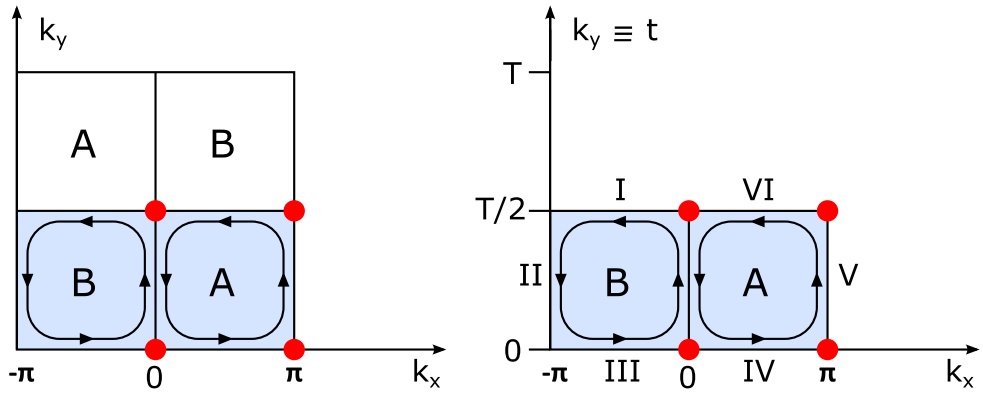

Figure 2.6: The Brillouin zone with periodic boundaries for a time reversal invariant insulator. The torus is split up into two regions: A and B. The red dots mark the four time reversal invariant points in the Brillouin zone. Due to time reversal symmetry all information is already contained in only half of the Brillouin zone (light blue), which is shown separately on the right. A closed integration path around the Brillouin zone is denoted by the segments I,II,III,IV,V and VI.

electrons. The insight from Kane and Mele was that, If $\nu = 1$, i.e. a topological insulator, then the $2N$ wavefunctions of a global basis cannot be divided into two groups (I and II) such that the two are related by time reversal symmetry as in equation 2.57 and 2.58. To see how ν is defined, let's consider a system that has time reversal symmetry but no spin-orbit coupling. In this case the two doublets I and II can be replaced by spin-up $\uparrow$ and spin-down $\downarrow$ of the electrons:

$$|u_\alpha^\uparrow(-\mathbf{k})\rangle = \Theta|u_\alpha^\downarrow(\mathbf{k})\rangle \tag{2.59}$$

$$\Theta|u_\alpha^\uparrow(\mathbf{k})\rangle = -|u_\alpha^\downarrow(-\mathbf{k})\rangle \tag{2.60}$$

and these two constraints will always be true. Therefore we need spin-orbit coupling to formulate a constraint in the first place. Spin-orbit coupling implies, that the spin orientation of a particle depends on the particle's angular momentum. In figure 2.6 we see that the two regions A and B in the Brillouin zone are the same if $\mathbf{k} \rightarrow$ **-k**. Now we can define two smooth gauges for every region A and B separately and then bring them together to cover the entire Brillouin zone. The wave-

functions must follow the time reversal constraints in equation 2.57 and 2.58. Let $|u^S_\alpha(\mathbf{k},t)\rangle_A$ be smoothly defined in A and $|u^S_\alpha(\mathbf{k},t)\rangle_B$ in B. We already know the right prodecure from the IQHS. For the IQHE it was a laborious process to find the right Berry connection from the conductance. The same can be done for a topological insulator by considering the polarization as the physical parameter, as has been done by Fu and Kane who followed the Laughlin argument by defining a spin pump instead of a charge pump [10]. For the sake of simplicity, we jump right ahead and use the Berry connection on our Brillouin zone. Let's define the Berry connection for the two regions A and B:

$$\mathbf{A}^A = \sum_n \langle u_n | \nabla | u_n \rangle_A \tag{2.61}$$

$$\mathbf{A}^B = \sum_n \langle u_n | \nabla | u_n \rangle_B . \tag{2.62}$$

If we start with $|u_n\rangle_A$ or $|u_n\rangle_B$, both are well-defined in their own regions:

$$\oint_{\partial A} d\mathbf{k} \cdot \mathbf{A}^A = \iint_A dk_x dk_y \nabla \times \mathbf{A}^A \tag{2.63}$$

$$\oint_{\partial B} d\mathbf{k} \cdot \mathbf{A}^B = \iint_B dk_x dk_y \nabla \times \mathbf{A}^B. \tag{2.64}$$

The problem is now that $|u_n\rangle_B$ is not defined in A and vice versa, thus we must find a connection between these two regions that allows us to integrate over the entire half Brillouin zone as shown in figure 2.6. Let's define:

$$\oint_{\partial A} d\mathbf{k} \cdot \mathbf{A}^B = \oint_{\partial(A+B)} d\mathbf{k} \cdot \mathbf{A}^B - \oint_{\partial B} d\mathbf{k} \cdot \mathbf{A}^B \tag{2.65}$$

$$= \oint_{\partial(A+B)} d\mathbf{k} \cdot \mathbf{A}^B - \iint_B dk_x dk_y \nabla \times \mathbf{A}^B. \tag{2.66}$$

Just like for the IQHS, a topological invariant can now be defined, but instead of a Chern invariant, we get a Chern parity:

$$\begin{aligned}
\nu &= \frac{1}{2\pi}\oint_{\partial A} d\mathbf{k}\cdot\left(\mathbf{A}^B-\mathbf{A}^A\right) && (2.67)\\
&= \frac{1}{2\pi}\left(\oint_{\partial(A+B)} d\mathbf{k}\cdot\mathbf{A}^B-\iint_B dk_x dk_y \nabla\times\mathbf{A}^B-\iint_A dk_x dk_y \nabla\times\mathbf{A}^A\right) && (2.68)\\
&= \frac{1}{2\pi}\left(\oint_{\partial(A+B)} d\mathbf{k}\cdot\mathbf{A}^B-\iint_{A+B} dk_x dk_y \nabla\times\mathbf{A}\right), && (2.69)
\end{aligned}$$

where in the last line we have used the fact that a gauge transformation does not affect: $\nabla\times\mathbf{A}^B = \nabla\times\mathbf{A}^A = \nabla\times\mathbf{A}$. Equation 2.79 does not contain much valuable information yet but it can be shown that this equation is gauge invariant only modulo 2 which will define the Z_2 invariant for topological insulators. To see why this is true let's consider the intregration path around the BZ in figure 2.6, where k_y is parameterized as T. We integrate around the entire BZ starting from I over II, III, IV and V until we close the integration path in VI. Now, time reversal symmetry gives a direct connection between pairs of these integration paths, i.e. I is the time reverse of VI, III of IV and II of V. This connection allows us to write:

$$\begin{aligned}
\oint_{\partial(A+B)} d\mathbf{k}\cdot\mathbf{A}^B = &\int_0^{-\pi}\left(\mathbf{A}^B\left(k,\frac{T}{2}\right)+\mathbf{A}^B\left(-k,\frac{T}{2}\right)\right)+\int_{-\pi}^{0}\left(\mathbf{A}^B(k,0)+\mathbf{A}^B(-k,0)\right)\\
&+\int_0^{T}\left(\mathbf{A}^B\left(\pi,\frac{T}{2}\right)+\mathbf{A}^B\left(-\pi,\frac{T}{2}\right)\right) \qquad (2.70)
\end{aligned}$$

where it is also true that:

$$\mathbf{A}^B\left(-k,\frac{T}{2}\right)=-\sum_n\left\langle u_n^B\left(-k,\frac{T}{2}\right)\middle|\nabla\middle|u_n^B\left(-k,\frac{T}{2}\right)\right\rangle=\mathbf{A}^B\left(k,\frac{T}{2}\right). \tag{2.71}$$

where a gauge transformation of one doublet of the Kramers' pair $u^I(k,t)\rightarrow e^{i\theta_k}u^I(k,t)$ is not independent of the other doublet: $u^{II}(-k,-t)\rightarrow e^{i\theta_k}u^{II}(-k,-t)$, but we must add these two Kramers' doublets to get the full vector potential. Therefore we can take the new transformation

$$\oint_{\partial(A+B)}d\mathbf{k}\cdot\mathbf{A}^B\rightarrow\oint_{\partial(A+B)}d\mathbf{k}\cdot\mathbf{A}^B+2\oint_{\partial(A+B)}d\mathbf{k}\cdot\nabla\theta_{\mathbf{k}} \tag{2.72}$$

modulo two and write $\mathbf{A}$ instead of $\mathbf{A}^B$. This definition, as an obstruction to Stokes' theorem, is completely equivalent to counting the number of zeros of the Pfaffian matrix as it is shown in [4]. The new invariant can be written as:

$$\nu=\frac{1}{2\pi}\left(\oint_{\partial(A+B)}d\mathbf{k}\cdot\mathbf{A}-\iint_{A+B}dk_xdk_y\nabla\times\mathbf{A}\right)\ (\mathrm{mod}\ 2). \tag{2.73}$$

The Chern invariant ν is easier to determine if we have inversion symmetry. If we have inversion symmetry we can follow a simplified argument from Fu and Kane to directly calculate ν from band structure calculations only by knowing the parity of the 2D Bloch states. At the time reversal invariant points, the Bloch states will be eigenstates of parity with an eigenvalue +1 or -1 [12]. Multiplying all these eigenvalues together, directly gives us ν.

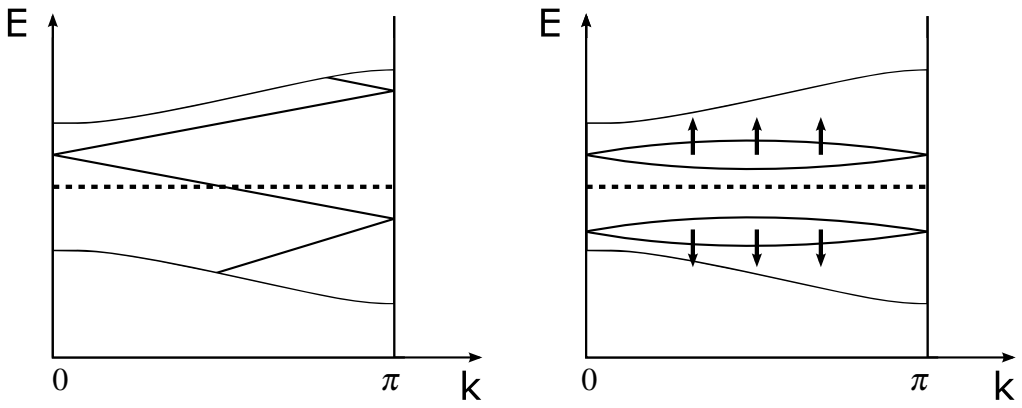

Figure 2.7: Two different ways how the energy bands can cross the Fermi energy (dotted line). At the time reversal invariant points (k = 0 = π), the states have to be doubly degenerate. In between these points, spin orbit interactions lift this degeneracy. A topological insulator has an odd number of Fermi crossings whereas a trivial insulator has an even number of Fermi crossings where the energy bands can be shifted out of the gap into the valence or conduction band by a small perturbation.

2.1.4 3D Topological Insulators

Similar to the 2D case, the 3D case can be considered as a stack of 2D topological insulators to form a 3D topological insulator. Instead of only one topological invariant ν in two dimensions we now have four topological invariants in three dimensions, $\nu_0;(\nu_1\nu_2\nu_3)$, where each of them can be either 0 or 1. If one of them is nonzero we speak of a three dimensional topological insulator. $\nu_0 = 1$ describes a strong topological insulator, whereas $\nu_0 = 0$ describes a weak topological insulator. These topological invariants are calculated in the same manner as shown in the last section. We will focus on the case where $\nu_0 = 1$, since in the experiment I will employ Bi_2Se_3, a strong topological insulator. Kramers' theorem only protects one twofold degeneracy, therefore all the other bands can be pushed away. The bulk boundary correspondence ensures the existence of surface states if the topological classification changes at this surface, e.g. from $\nu_0 = 1$ for a TI into $\nu = 0$ for vacuum. Let's assume we have a valence band and a conduction band of our topological insulator. Due to Kramer's pairs and TR-symmetry we know that the existing surface states have

to be degenerate at the points with time-reversal symmetry. Due to the spin-orbit interaction, this degeneracy has to split up when we leave these points. We can invoke topology and consider the number of crossings of these states with the Fermi energy and see that it comes back to our notion of odd and even connections that was introduced in the Koenigsberg bridge problem. This translates back to the parity introduced in the Koenigsberg problem. It distinguishes between bands with two open ends where one must end in the valence and the other one in the conduction band or a closed loop that can be pushed into the bulk bands if the Hamiltonian is disturbed. Fu and Kane compared different paths of the wavefunction around the time reversal invariant points and found that for the non-trivial topology with a Berry phase of π and the strong topological insulator with $\nu_0 = 1$, the wavefunctions must wind around a single time reversal point in the Brillouin zone [12]. This leads to a Dirac-like dispersion relation and to one single crossing of the Fermi energy.

2.1.5 Majorana Fermions

Although this thesis is not directly related to Majorana fermions it serves as a motivation why current research is interested in topological superconductors or topological insulators and their combination with s-wave superconductors. Both can create so called Majorana zero modes that have non-abelian statistics and can be used in quantum computing [16].

In 1928 Dirac proposed a relativistic wave equation for fermions:

$$(i\gamma^{\mu}\partial_{\mu} - m)\Psi = 0 \tag{2.74}$$

where m is the mass of the fermion. Dirac described a set of γ matrices for a complex field that describes charged fermions, therefore a charged particle is not its own antiparticle under complex

conjugation:

$$\Psi \neq \Psi^*. \tag{2.75}$$

In 1937 Majorana asked the question if instead of a complex field for charged fermions there could be a real field and he proposed new imaginary γ matrices that now lead to the possibility that a particle can be its own antiparticle:

$$\Psi = \Psi^*. \tag{2.76}$$

This proposed particle, in the honor of Ettore Majorana, is called *Majorana fermion*. In particle physics there has been an ongoing search for Majorana fermions and researchers believe that the Neutrino might be one. In a conventional double beta decay, two neutrons decay into two protons, two antineutrinos and two electrons. If a neutrinoless double-beta decay is observed in nature then this would be a proof for the neutrino being a Majorana fermion, because a neutrino and an antineutrino can annihilate in this process whereas in a normal double-beta decay, two antineutrinos won't be able to annihilate each other. Current Research suggests that neutrinos have mass and this is a first step to show that indeed a neutrino can become an antineutrino and vice versa. But the neutrino is notoriously difficult to detect and the proof will probably not be possible in the near future.

Condensed matter physics like particle physics offers a rich variety of particles, not in terms of elementary particles but in terms of quasiparticles. We could ask the question if there are quasiparticle excitations that behave like Majorana fermions in condensed matter physics. It is convenient to describe these particles as excitations in the language of second quantization. $c_j^\dagger$ is a creation operator of a particle (electron) and c_j an annihilation operator or the creation operator of an antiparticle (hole), where j denotes other quantum numbers such as the momentum. These operators have to obey Fermi-Dirac statistics, i.e. no two electrons or holes can occupy the same

state ($(c_j^\dagger)^2 = c_j^2 = 0$), whereas antisymmetry and completeness of these two operators are the two other requirements. The simplest particle to start with is an electron. So, we can ask the question if an electron is in fact equal to a hole and therefore a Majorana fermion:

$$c_j \stackrel{?}{=} c_j^\dagger. \tag{2.77}$$

Both, the elctron and hole are fermions but clearly they are not equal to each other because of their charge. If these two don't work, we could consider their combination. This combination is called an exciton:

$$c_j c_k^\dagger + c_j^\dagger c_k \stackrel{?}{=} c_j^\dagger c_k + c_j c_k^\dagger. \tag{2.78}$$

The charge does not play a role anymore but this combination is not a fermion but a boson with integer spin, therefore the Dirac equation is not valid. Fortunately another promising quasiparticle excitation can be found in superconductors:

$$c_j^\dagger + c_k \stackrel{?}{=} c_j + c_k^\dagger \tag{2.79}$$

From equation 2.79 we see that under complex conjugation the charge does not change and the linear combination still obeys the fermionic anticommutation relation. But there is still one catch that will become obvious when we consider a Bogoliubov transformation. A Bogoliubov transformation preserves the fermionic anticommutation relations under a unitary transformation and is used to find the solutions in BCS theory when the BCS-Hamiltonian is diagonalized.

We start with the known fermionic anticommutation relation for our creation and annihilation operators:

$$\left\{c, c^\dagger\right\} = 1 \tag{2.80}$$

and we define a new pair of operators that are in fact the quasiparticle excitations:

$$\gamma = uc + vc^\dagger \tag{2.81}$$

$$\gamma^\dagger = u^* c^\dagger + v^* c \tag{2.82}$$

that must still satisfy the fermionic anticommutation relation

$$\left\{\gamma, \gamma^\dagger\right\} = 1. \tag{2.83}$$

Now we check what we must choose for the constants u and v, for the transformation to remain canonical:

$$\left\{\gamma, \gamma^\dagger\right\} = \left\{uc + vc^\dagger, u^* c^\dagger + v^* c\right\} = \left(|u|^2 + |v|^2\right)\left\{c, c^\dagger\right\} = \left\{c, c^\dagger\right\} \tag{2.84}$$

where we see that $\left(|u|^2 + |v|^2\right)$ must be equal to one. This condition can be parametrized as:

$$u = e^{i\theta 1}\cos(\phi) \tag{2.85}$$

$$v = e^{i\theta 2}\sin(\phi) \tag{2.86}$$

so that we get:

$$\gamma = e^{i\theta 1}\cos(\phi)c_j + e^{i\theta 2}\sin(\phi)c_k^\dagger. \tag{2.87}$$

We now have another constraint if we want to enforce the requirement for a Majorana fermion $\gamma = \gamma^\dagger$. In particular, it is obvious that $\cos(\phi)$ and $\sin(\phi)$ must be equal, which is true for e.g. $\phi = \frac{\pi}{4}, \frac{5\pi}{4}, \ldots$. This constraint can be encoded in the angular direction of the pairing of the elec-

tron $c^\dagger$ and the hole c in terms of their momentum and spin, and gives a first hint why we distinguish between a s-wave superconductor that has a spherical symmetry or a p-wave superconductor that breaks this spherical symmetry. To be more precise, this information can be encoded in the superconducting order parameter Δ. The spin-momentum locking of the surface states in a 3D topological insulator is a suitable constraint and will be utilized in the next subsection.

2.1.6 P-wave superconductivity

It was soon to be realized that the particle hole symmetry for a conventional s-wave BCS superconductor creates the same Hamiltonian that is produced by time reversal symmetry for a topological insulator. Therefore the notion of a topological superconductor was born, because the same arguments developed earlier can now be applied for a system with particle hole symmetry. In the previous subsection about Majorana fermions we gave an intuitive motivation why we want a p-wave superconductor instead of a s-wave superconductor. Common low temperature superconductors such as lead and niobium are conventional s-wave superconductors and current research results suggest that high-temperature superconductors don't rely on s-wave pairing but on d-wave. Unfortunately there is no natural p-wave superconductor available except a few candidates such as Sr_2RuO_4 or the He-3 superfluid phase.

Since nature has not yet given us a suitable p-wave superconductor, mankind must create one, and two approaches have already been proposed: One way to engineer an artificial p-wave superconductor is to bring a conventional s-wave superconductor close to a material that has a strong spin-orbit coupling to avoid spin-degeneracy (Rashba spin-splitting) and expose it to a magnetic field. A suitable material is the semiconductor InAs, which already gave some promising results in 2012 [23]. The second way, which will be used in this thesis, was proposed by Charles Kane and Liang Fu earlier in 2007; They suggested to deposit a conventional s-wave superconductor on the

surface of a topological insulator [11].

To understand their motivation, let's consider the pairing object in the Hamiltonian of a conventional s-wave superconductor:

$$\sum_{\mathbf{k}} \Delta_{\mathbf{k}} c^{\dagger}_{\uparrow\mathbf{k}} c^{\dagger}_{\downarrow -\mathbf{k}}, \tag{2.88}$$

where the sum goes over all values of $\mathbf{k}$. $\mathbf{k}$ is the momentum of the electron and the arrows denote its spin. Under inversion $\mathbf{k} \to -\mathbf{k}$ we have:

$$\sum_{\mathbf{k}} \Delta_{\mathbf{k}} c^{\dagger}_{\uparrow\mathbf{k}} c^{\dagger}_{\downarrow -\mathbf{k}} \quad \to \quad \sum_{\mathbf{k}} \Delta_{-\mathbf{k}} c^{\dagger}_{\uparrow -\mathbf{k}} c^{\dagger}_{\downarrow\mathbf{k}} = -\sum_{\mathbf{k}} \Delta_{-\mathbf{k}} c^{\dagger}_{\downarrow\mathbf{k}} c^{\dagger}_{\uparrow -\mathbf{k}}, \tag{2.89}$$

where we made use of the fermionic anticommutation relation: $c^{\dagger}_{\uparrow -\mathbf{k}} c^{\dagger}_{\downarrow\mathbf{k}} = -c^{\dagger}_{\downarrow\mathbf{k}} c^{\dagger}_{\uparrow -\mathbf{k}}$. Now, because of the fact that the spin is explicitly in this equation, there is no relation for $\Delta_{\mathbf{k}}$ under inversion and we can set the value of $\Delta_{\mathbf{k}}$ independent of $\mathbf{k}$ or **-k**:

$$\Delta_{\mathbf{k}} = \Delta_{-\mathbf{k}} = \text{some constant}. \tag{2.90}$$

Let's see what would happen if we do not include spin. One way to create so called *spinless* electrons is to isolate up-spin and down-spin electrons from each other, e.g. by a strong magnetic field. That is also the reason why a *normal* p-wave superconductor has inherently broken time reversal symmetry. The spinless case is:

$$\sum_{\mathbf{k}} \Delta_{\mathbf{k}} c^{\dagger}_{\mathbf{k}} c^{\dagger}_{-\mathbf{k}}. \tag{2.91}$$

Under inversion $\mathbf{k} \to -\mathbf{k}$ we then have:

$$\sum_{\mathbf{k}} \Delta_{\mathbf{k}} c^{\dagger}_{\mathbf{k}} c^{\dagger}_{-\mathbf{k}} \quad \to \quad \sum_{\mathbf{k}} \Delta_{-\mathbf{k}} c^{\dagger}_{-\mathbf{k}} c^{\dagger}_{\mathbf{k}} = -\sum_{\mathbf{k}} \Delta_{-\mathbf{k}} c^{\dagger}_{\mathbf{k}} c^{\dagger}_{-\mathbf{k}}. \tag{2.92}$$

This spinless case is a p-wave superconductor because the eigenvalue of $\Delta_{\mathbf{k}}$ under inversion is -1:

$$\Delta_{\mathbf{k}} = -\Delta_{-\mathbf{k}}. \tag{2.93}$$

Fu and Kane proposed to deposit a s-wave superconductor on the surface of a strong 3D topological insulator where Cooper pairs will travel from the s-wave superconductor into the surface states of the topological insulator. The addition of the Cooper pairs into the surface states can be described by adding

$$V = \Delta_0 e^{i\phi} \psi^{\dagger}_{\uparrow} \psi^{\dagger}_{\downarrow} + (h.c.) \tag{2.94}$$

to the surface Hamiltonian of the topological insulator, where the hermitian conjugate will be left out for simplicity. Next we define new operators that are a superposition of a state $\uparrow \mathbf{k}$ with a state $\downarrow \mathbf{k}$

$$c_{\mathbf{k}} = \frac{\psi_{\uparrow \mathbf{k}} + e^{i\theta_{\mathbf{k}}} \psi_{\downarrow \mathbf{k}}}{\sqrt{2}} \tag{2.95}$$

where θ is the angle of the vector $\mathbf{k}$ going around the Dirac point: $\mathbf{k} = k_0(\cos\theta_{\mathbf{k}}, \sin\theta_{\mathbf{k}})$. Thus we have created a formal equivalent to a spinless (or spin polarized) p-wave superconductor and the new Hamiltonian does indeed resemble one:

$$\sum_{\mathbf{k}} \Delta_{\mathbf{k}} e^{i\theta_{\mathbf{k}}} c^{\dagger}_{\mathbf{k}} c^{\dagger}_{-\mathbf{k}}. \tag{2.96}$$

Although it looks like a p-wave superconductor it is not a p-wave superconductor since the order

parameter is still even and it does not violate time reversal symmetry. Under inversion $\mathbf{k} \to -\mathbf{k}$ we get

$$\sum_{\mathbf{k}} \Delta_0 e^{i\theta_{\mathbf{k}}} c^\dagger_{\mathbf{k}} c^\dagger_{-\mathbf{k}} \quad \to \quad \sum_{\mathbf{k}} \Delta_0 e^{i\theta_{-\mathbf{k}}} c^\dagger_{-\mathbf{k}} c^\dagger_{\mathbf{k}} = -\sum_{\mathbf{k}} \Delta_0 e^{i\theta_{-\mathbf{k}}} c^\dagger_{\mathbf{k}} c^\dagger_{-\mathbf{k}} = \sum_{\mathbf{k}} \Delta_0 e^{i\theta_{\mathbf{k}}} c^\dagger_{\mathbf{k}} c^\dagger_{-\mathbf{k}}, \tag{2.97}$$

where now the minus sign from the fermionic anticommutation relation got eliminated by a phase of π:

$$-e^{i\theta_{-\mathbf{k}}} = -e^{i(\theta_{\mathbf{k}}+\pi)} = -e^{i\theta_{\mathbf{k}}} e^{i\pi} = e^{i\theta_{\mathbf{k}}}. \tag{2.98}$$

Time reversal acting on our new operators gives

$$\Theta c \Theta^{-1} = \frac{\psi_{\downarrow \text{-}\mathbf{k}} - e^{-i\theta_{\mathbf{k}}} \psi_{\uparrow \text{-}\mathbf{k}}}{\sqrt{2}} = \frac{-e^{-i\theta_{\mathbf{k}}} (\psi_{\uparrow \text{-}\mathbf{k}} - e^{i\theta_{\mathbf{k}}} \psi_{\downarrow \text{-}\mathbf{k}})}{\sqrt{2}} = -e^{-i\theta_{\mathbf{k}}} c_{-\mathbf{k}} \tag{2.99}$$

$$\Theta c^\dagger_{\mathbf{k}} \Theta^{-1} = -e^{i\theta_{\mathbf{k}}} c^\dagger_{-\mathbf{k}} \tag{2.100}$$

$$\Theta c^\dagger_{-\mathbf{k}} \Theta^{-1} = -e^{i\theta_{-\mathbf{k}}} c^\dagger_{\mathbf{k}}, \tag{2.101}$$

which will lead to

$$\Theta \left(\sum_{\mathbf{k}} \Delta_0 e^{i\theta_{\mathbf{k}}} c^\dagger_{\mathbf{k}} c^\dagger_{\text{-}\mathbf{k}} \right) \Theta^{-1} = \sum_{\mathbf{k}} \Delta_0 e^{i\theta_{-\mathbf{k}}} c^\dagger_{\text{-}\mathbf{k}} c^\dagger_{\mathbf{k}} = \sum_{\mathbf{k}} \Delta_0 e^{i\theta_{\mathbf{k}}} c^\dagger_{\mathbf{k}} c^\dagger_{\text{-}\mathbf{k}}. \tag{2.102}$$

Therefore the system obeys time reversal symmetry unlike a real p-wave superconductor. Unlike an intrinsic 3D topological superconductor such as the candidate $Cu_xBi_2Se_3$ that (in theory) has Majorana fermions living on its surface[3], a 3D topological insulator combined with a s-wave superconductor creates a 2D topological superconductor where Majorana fermions live at its edge.

[3]Recent published results such as a point contact spectroscopy experiment report signatures of Majorana fermions in terms of a zero bias conductance peak in the density of states [38] [30].

In order to measure a Majorana bound state, it is therefore not enough to just measure the density of states at the surface, but to probe the edges of the surface, e.g. by having a hole in the s-wave superconductor as proposed by Kane and Fu. Additionally, one needs to pin a Majorana bound state down to zero energy, which can be achieved by sending magnetic flux through this hole that is similar to a vortex in a p-wave superconductor.

2.2 Theory of Scanning Tunneling Microscopy and Spectroscopy

"Tunneling is an art, not a science"[4]

Scanning Tunneling Microscopy (STM) was successfully developed by Binnig and Rohrer in 1982 [BR] and was rewarded with the Nobel price in physics as it has led to new breakthroughs in surface science. STM gives insight in the topography, i.e. the structural properties of a conducting sample surface down to the atomic scale while Scanning Tunneling Spectroscopy (STS) can simultaneously observe the local density of states. A lot of fascinating improvements and techniques have been developed over the past few decades such as Fourier-Transform Scanning Tunneling Microscopy (FT-STM) and Spin-Polarized Scanning Tunneling Microscopy (SP-STM). To probe the superconducting proximity effect in this thesis experiment, we will focus on STM and STS. Using a Scanning Tunneling Microscope has the advantage that we can directly probe the surface states which is especially important for topological insulators since the surface states live on the surface. I believe it is of paramount importance to combine STS studies with other experiments such as Angle Resolved Photoemission Spectroscopy (ARPES) or FT-STM to complete and support the STS data and to get a complete picture of the electrons in momentum space.

All of the following calculations are based on the description given in the renowned STM introduction by Stroscio [STROS] who followed the arguments of Tersoff, Lang, Hamann and Selloni. We start by considering the actual tunneling junction in the STM: the tip and sample are the two electrodes that are separated by an insulating layer, i.e. the vacuum barrier. When brought close to each other ($\sim$ 1 Å), electrons will begin to tunnel from the tip into the sample and vice versa. Without a voltage no net tunneling current will be observed since the two Fermi levels, both

[4] A remark about the uncountable influences in Scanning Tunneling Spectroscopy that can lead to non-reproducibility in data, by Stroscio [STROS] who cites C.B. Duke.

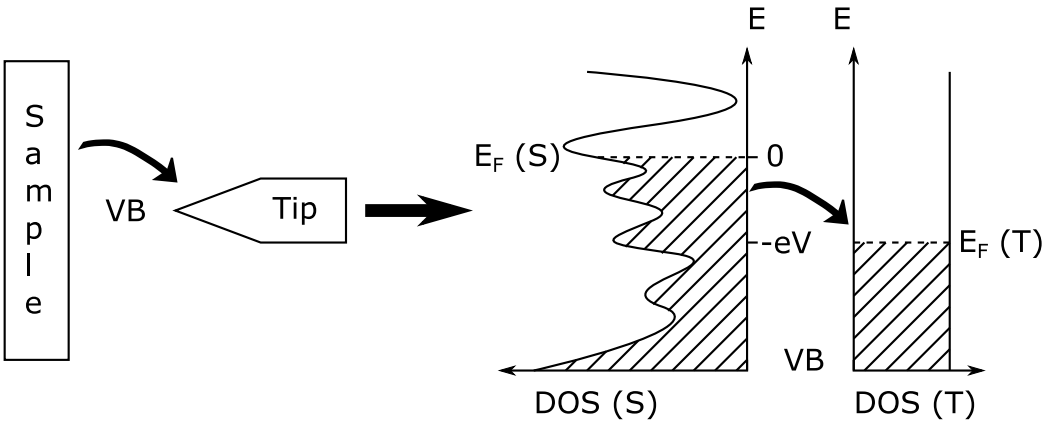

Figure 2.8: Sketch of tunneling between tip and sample with a negative applied voltage to the sample. Left: The vacuum barrier (VB) seperates the tip from the sample and creates a tunneling junction. Right: Density of states (DOS) of both the sample (S) and the tip (T). The negative voltage lifts the Fermi energy of the sample up by eV and electrons can tunnel from the sample to the tip creating an observable tunneling current.

of the tip and the sample, will equilibrate to the same energy level. In order to achieve a constant tunneling current, a voltage between the tip and the sample is applied. The tip is attached to piezo tubes that allow it to navigate the tip in x,y and z-direction. This also allows to scan over the surface while keeping the tunneling current constant with a feedback loop that automatically extends or retracts the tip as the tunneling current de- or increases. Solving the Schroedinger equation for a one-dimensional potential barrier one can easily provide an estimate for the spatial dependence of the tunneling current in the z-direction, perpendicular to the surface:

$$I \propto |\phi|^2 = e^{-2\kappa d} \tag{2.103}$$

where ϕ is the wavefunction of the surface conduction electrons, $\kappa = \frac{2m}{\hbar^2}(V_B - E)$ where V_B here refers to the energy of the barrier (e.g. workfunction), and d is the distance between the sample and tip. This exponential dependence results in observable changes of either the current when d

is changed or vice versa. A more advanced, but still simplified[5], picture of the tunneling barrier between the tip and sample was given in [14]. We assume a weak tip-sample coupling and low voltages that can be treated with first order perturbation theory. The tunneling current is then:

$$I = \frac{4\pi e}{\hbar}\int_{-\infty}^{\infty} d\varepsilon[f(E_F - eV + \varepsilon) - f(E_F + \varepsilon)]\rho_{tip}(E_F - eV + \varepsilon)\rho_{sample}(E_F + \varepsilon)|M|^2 \quad (2.104)$$

where eV is the potential difference between the sample and the tip. $f(E)$ is the Fermi function with E_F being the Fermi energy. $\rho(E)$ is the density of states, ε the energy of the electrons and M is the tunneling matrix element. At low temperatures this equation can be approximated as:

$$I = \frac{4\pi e}{\hbar}\int_{0}^{eV} d\varepsilon\rho_{tip}(E_F - eV + \varepsilon)\rho_{sample}(E_F + \varepsilon)|M|^2. \quad (2.105)$$

If the density of states of the tip is constant over low applied voltages it can be further simplified to:

$$I \approx \frac{4\pi e}{\hbar}|M|^2\int_{0}^{eV} d\varepsilon\rho_{sample}(E_F - eV + \varepsilon). \quad (2.106)$$

and therefore we have a direct proportionality to the density of states of the sample that lie between the Fermi energy and the applied voltage:

$$I \propto \int_{0}^{eV} \rho_{sample}(E_F + \varepsilon)d\varepsilon. \quad (2.107)$$

[5]The shape of the tip and, the wavefunction of the last atom on the tip where the tunneling current is going through, i.e. s-wave, p-wave..., the influence of the proximity of the tip on the sample and higher voltages applied to the system are all things that are not described.

The derivative of equation 2.107 is directly proportional to the density of states of the sample:

$$\frac{dI}{dV} \propto \rho_{sample}(E_F + eV). \tag{2.108}$$

For point spectroscopy the tip is positioned over the area of interest and the feedback loop is turned off. Now the voltage can be swept over a predefined range and a change in voltage V usually leads to a change in current I to yield a so called $I-V$ curve. This curve can be numerically differentiated to obtain the derivative dI/dV that is proportional to the density of states. This technique can be enhanced by using a lock-in amplifier. The method employs a small sinusoidal oscillation added to the voltage that is typically in the range of a few millivolts. The output of the lock-in is essentially dI/dV with a significantly improved signal-to-noise ration compared to the standard technique.

2.3 Probing the superconducting proximity effect with Scanning Tunneling Spectroscopy

Since STS can directly probe the density of states, especially at low voltages, it is an ideal device to investigate the superconducting density of states, where the superconducting order parameter Δ is normally in the range of a few meV.

2.3.1 Spatial dependence of the order parameter Δ

Since experiments and theoretical calculations (e.g. our last experiment by Dr. Romanowich [29] showed an offset due to bulk states) suggest that the surface states coexist with bulk states, I will not assume the clean limit. Instead I will desribe the dirty limit as a first simple description of the proximity effect. The Tessmer group has a rich experience in probing the superconducting proximity effect. Dr. Tessmer himself probed the proximity effect across a normal metal-superconductor interface on $NbSe_2$, where Au islands were evaporated on the surface of a superconducting $NbSe_2$ crystal [33]. If we have a good electrical contact between the superconductor (S) and the normal metal (N) then Cooper pairs will travel from S to N. Hence superconductivity is weakened in S and induced in N. Superconductivity in N will weaken with an increasing distance from S, since scattering events in N are causing the Cooper pairs to lose coherence.

In 1964 the Russian physicist Andreev described the so called Andreev reflection that plays an important role for the proximity effect. An electron with an energy less than the superconducting energy gap approaching S from N will not find a single state in S to go into. It will therefore reflect as a hole with opposite spin and momentum while one Cooper pair is added to the condensate, as one Cooper pair is basically one electron and one hole. The incoming electron in N and the reflected hole are weakly coupled and are exhibiting a weak superconducting pairing correlation

in proximity to S. In the dirty limit, the proximity can be described by a length scale ζ which for a normal metal in thermal equilibrium [9]:

$$\zeta_{\mathrm{N}} = \sqrt{\frac{\hbar D}{k_B T}} \tag{2.109}$$

where $\hbar$ is the Planck constant, T the temperature, k_B the Boltzmann constant and D the diffusion constant of the electrons. In this first simple approximation, ζ_{N} decreases with T and increases with D. The decrease of the superconductivity in S can be described with a different length scale ζ_{S}. The entire proximity effect over S and N can be formally described in the BCS framework by two parameters: The pair correlation amplitude F and the effective pairing interaction constant g leading to a spatially dependent BCS order parameter $\Delta(x) = gF(x)$, where g is usually approximated as a step function across the interface.

The intrinsic properties of N are crucial for the proximity effect. One can ask the question what happens if only certain states in N such as the surface states in a topological insulator are available for the Cooper pairs to enter. Since pure surface states provide no backscattering channels but only ballistic transport, ζ_{N} should be significantly enhanced. The aim of this thesis experiment is to probe the length scale ζ_{N} and the interplay of the surface states with the coexisting bulk states by measuring the spatial dependence of the superconducting order parameter Δ as shown in figure 2.9. This can be directly extracted from the width of the superconducting gap in the density of states, that is equal to 2Δ in the zero-temperature limit.

It is not yet understood how bulk states in the topological insulator that are present with the surface states will affect this transport. Not only is it not understood, but it also is an important question because most recent studies blame the coexisting bulk states for the suppression of exotic properties such as the emergence of Majorana fermions whereas other experiments claim that the

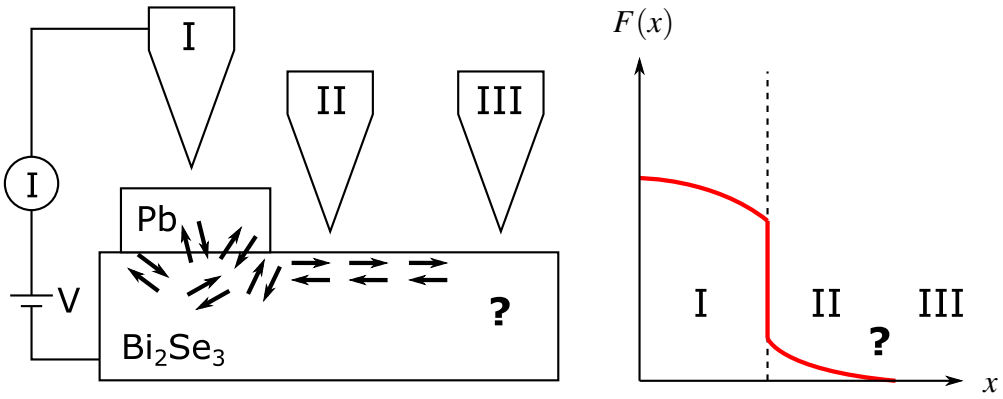

Figure 2.9: Schematics of the proposed thesis experiment. A superconducting island (Pb or Nb) is deposited on the surface of a topological insulator (Bi_2Se_3). We investigate the density of states with STS at different positions. When the tip is directly placed above the island (position I) we expect to see a superconducting gap 2Δ. At position II we expect to see a decreasing superconducting gap, i.e. a decrease of the order parameter Δ and at position III we expect to see no more superconducting gap but only the surface states of the topological insulator. The arrows and their rotational arrangement sketch the s-wave and p-wave characteristics of the superconducting order parameter Δ.

helical structure of the surface electrons is not disturbed by the bulk states [39].

A very similar experiment has recently been done by a research group, that has grown Bi_2Se_3 thin films on top of a $NbSe_2$ crystal. [36]. They found that the Cooper pair formation persists from one quintuple layer up to seven quintuple layers of Bi_2Se_3 until topological order dominates. These results were interesting in terms of the bulk states in Bi_2Se_3, but this experiment differed from our experiment, because they only probed the superconducting proximity effect in z-direction, through the bulk and not in the lateral x- direction where Cooper pairs can travel into the surface states and $F(x)$ can be explicitly probed.

Progress has already been made in transport experiments (non STM) that also probed the superconducting proximity effect of different s-wave superconductors (Sn, Al, Pb, Nb, NbN, Bi) deposited on Bi_2Se_3 or Bi_2Te_3 and either reported zero conductance peaks due to the assumed but not yet proven presence of Majorana bound states, direct confirmation of p-wave superconduc-

tivity, an observation of a proximity induced supercurrent or perfect Andreev reflection: [19] [28] [40] [41] [7] [39].

Chapter 3

Experiment

This chapter discusses every step necessary to investigate superconducting structures on top of a topological insulator with STM. It starts by describing the growth process of the Bi_2Se_3 crystals and continues with our available processing methods to deposit superconductors on top of the crystal surface. The first method is sputtering for Nb and the second is thermal evaporation for Pb or PbBi. Both methods investigated self-assembled island growth and a controlled patterned island growth using a shadow mask. Once the crystal is processed, we can investigate these new structures with a STM setup that is described in the last section of this chapter.

3.1 Crystal Growth

The samples were grown by the Kanatzidis group at Northwestern University. Appropiate weights of starting materials (bismuth and selenium) were mixed, placed into quartz tubes and sealed under vacuum ($1.0 \cdot 10^{-4}$ torr). These tubes were then slowly heated up to 850 $^{\circ}$C in a box furnace over 15 hours, where they were kept at 850 $^{\circ}$C for 10 hours and then cooled down to room temperature over a time period of 15 hours. Beside the common Bi_2Se_3 crystals, bismuth-excess samples were grown as well. Past STM experiments in the Tessmer group suggest that the $Bi_{2.04}Se_3$ (2% excess bismuth) sample worked best in terms of cleaving and stability, which is why we investigate $Bi_{2.04}Se_3$ instead of Bi_2Se_3. There is no guarantee that the excess bismuth is taken up by the crystal. An earlier unit cell analyis of our collaborateur showed nevertheless that the lattice of $Bi_{2.04}Se_3$ extended a bit compared to Bi_2Se_3 which is evidence that more bismuth was taken in by the lattice.

3.2 Nb Sputtering

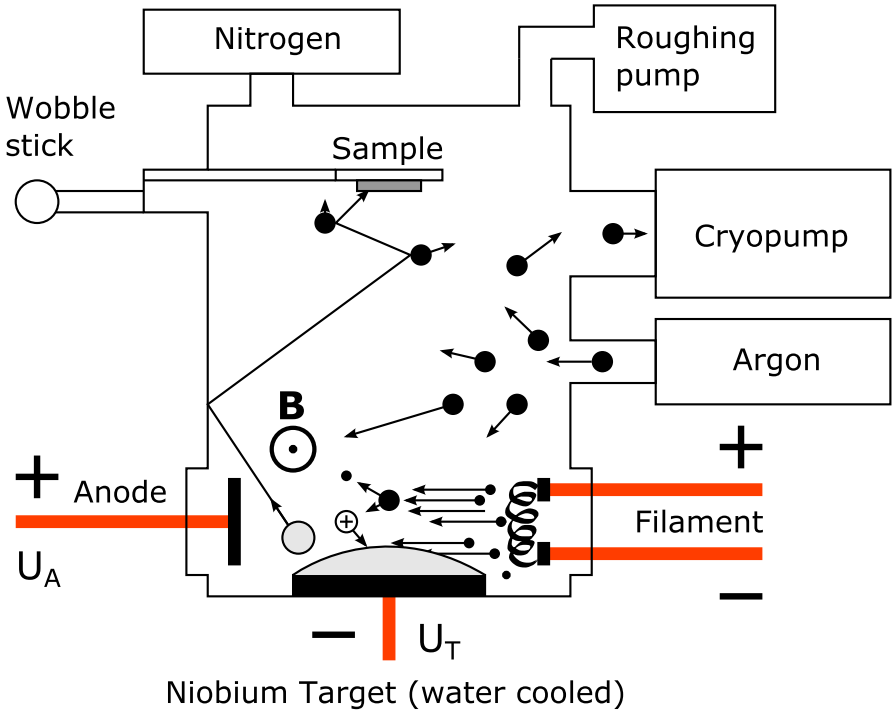

Figure 3.1: Basic components of a triode gun sputtering chamber. To show the pathways of the particles, a few of them inside the chamber are sketched. Thermally activated electrons are leaving the heated filament and are accelerated towards the anode that has an adjustable positive voltage $\mathbf{U}_\mathrm{A}$ (This acceleration is enhanced with a perpendicular magnetic field **B**, that will force the electrons and argon ions on a circular motion, hence increasing the impact probability of both the electrons with the argon atoms and the argon ions with the niobium target). A high negative voltage $\mathbf{U}_\mathrm{T}$ is also applied to the Nb target that attracts the argon ions and repels the electrons. When the argon gas is released, the electrons will ionize argon atoms close to the niobium target. The argon ions will eventually impact the niobium target that will then lead to sputtering of neutral niobium atoms. These atoms will scatter up to the sample surface where they condense.

Nb has a high melting point (2477 $^\circ$C) and thus cannot be easily thermally evaporated. A common physical vapor deposition technique to deposit Nb on surfaces is sputtering. Michigan State University has its own computer controlled DC triode sputtering system that was developed and optimized by Dr. R. Loloee and Dr. W. Pratt Jr.. To test how this Nb deposition technique works with Bi_2Se_3, a flat Bi_2Se_3 crystal was glued on a STM sample disk with silver paint,

cleaved in air and then put in the sample holder inside the sputtering chamber as shown in figure 3.1. The chamber was then pumped down to $1.0 \cdot 10^{-2}$ torr with a mechanical pump that serves as a roughing pump. After reaching this pressure, the roughing pump was sealed off by a gate valve and a cryopump was activated creating a pressure of about $8.0 \cdot 10^{-8}$ torr. This vacuum can be enhanced to $2.5 \cdot 10^{-8}$ torr by baking the chamber for 24 hours and filling a cold trap inside the chamber with liquid nitrogen to absorb molecules to its walls. Once a desirable high vacuum is reached, the entire sputtering chamber is backfilled with high purity Ar gas to about $2.5 \cdot 10^{-3}$ torr. The Ar atoms are now constantly flowing over the triode gun through the chamber into the cryopump. The filament of the triode gun is heated with a current **I** to release thermally activated electrons. Simultaneously a positive voltage $\mathbf{U_A}$ is applied to the anode opposite of the filament and a negative voltage $\mathbf{U_T}$ is applied to the Nb target. This accelerates the electrons towards the anode that then impact Ar atoms that are in their way close to the Nb target. The Ar atoms get ionized by the fast moving electrons and and the resulting positive Ar ions are accelerated towards the Nb target where they transfer their high kinetic energy to Nb atoms that then leave the Nb target and scatter their way through the chamber to the sample where they condense on the surface. A magnetic field **B**, that is perpendicular to the electric fields, forces the electrons and Ar ions on a circular path, hence enhancing the impact probability of both the electrons with the Ar atoms and the Ar ions with the Nb target. The chamber is vented with dry nitrogen gas after the sputtering process to reduce sample contamination.

This specific setup gives us a few parameters to play with in order to change the deposition rate, the number of scattering events or the kinetic energy of the arriving Nb atoms on the sample surface. These parameters are: The Ar gas pressure **P**, the anode voltage $\mathbf{U_A}$, the Nb target voltage $\mathbf{U_T}$ and the current through the filament **I**. The anode voltage $\mathbf{U_A}$ and the current through the filament **I** are usually combined to only one parameter, the plasma current $\mathbf{I_P}$, since both

parameters are directly related to the number of electrons and their acceleration leading to more or fewer Ar ions. The normal operational Ar gas pressure for the triode gun is about $2.5 \cdot 10^{-3}$ torr, the mininum pressure is $1.0 \cdot 10^{-4}$ torr and the maximum pressure is $5 \cdot 10^{-3}$ torr, where the increased number of scattering events of Nb atoms with the dominating Ar atoms won't allow a satisfying deposition anymore. The parameters $\mathbf{I_P}$ and $\mathbf{U_A}$ mostly change the deposition rate while $\mathbf{U_T}$ directly affects the kinetic energy of the arriving Nb atoms.

3.3 Pb/PbBi Evaporation

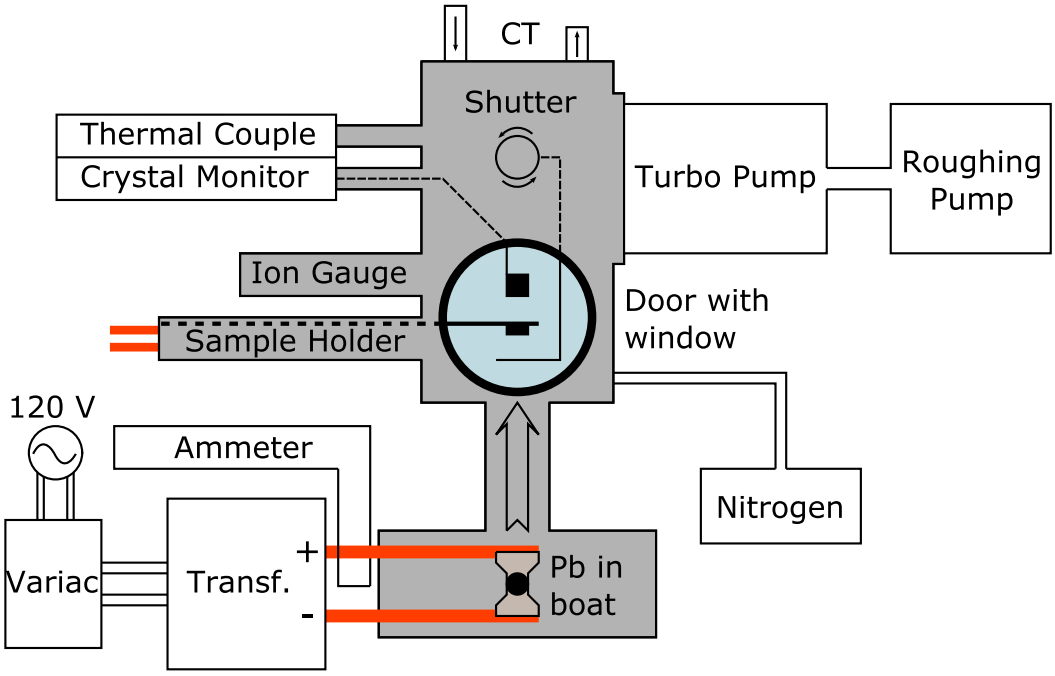

Figure 3.2: Basic components of the evaporation chamber. Two copper rods (orange) extend from the transformer into the UHV chamber (gray) and support a boat with lead in it. When the current through the boat is increased with the Variac, the lead begins to evaporate (represented by the arrow pointing upwards) and will condense on the surface of the Bi_2Se_3 crystal which is supported by the sample holder.

Unlike Nb, Pb is a soft material with a melting point of only 327.5 °C, and can easily be evaporated. Figure 3.2 shows the basic components of the evaporation chamber that had to be build for this thesis experiment to evaporate Pb or PbBi on a cleaved $Bi_{2.04}Se_3$ crystal. The chamber is always kept under a dry nitrogen environment which reduces the contamination of the sample when the chamber is vented and also reduces the pumpdown time. The $Bi_{2.04}Se_3$ crystal was glued onto a STM sample disk with high purity silver paint. After the silver paint dried, the crystal was cleaved in a nitrogen bag, secured in the sample holder and was transferred into the evaporation chamber as outlined in figure 3.3. The components of the sample holder have been cleaned by submerging them in alconox, acetone, isopropyl alcohol and dionized water, employing

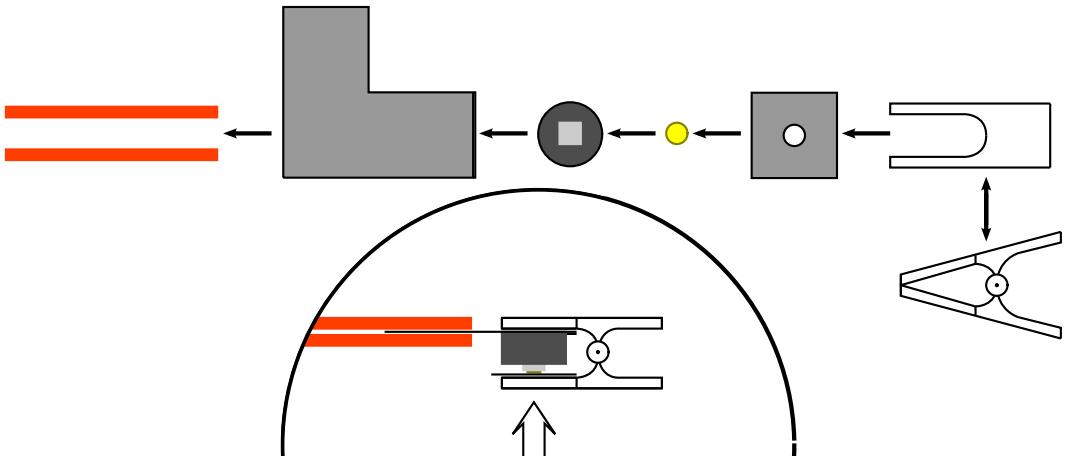

Figure 3.3: Basic components of the sample holder. Top: (from left to right) Copper rods for supporting the actual sample holder, Stainless steel bottom plate, STM disk with Bi_2Se_3 crystal, Golden shadow mask, Stainless steel top plate, Clamp. Bottom: Fully assembled sample holder inside the evaporation chamber as seen through the glass window.

an ultrasonic bath of 15 minutes for each solution, after which the components were blown dry with compressed nitrogen gas. The high nitrogen pressure inside the chamber made a transfer of the sample from the mobile nitrogen bag to the sample holder through the door possible without exposing the cleaved surface to air.

Once the sample is placed in the chamber, the mechanical pump is turned on and creates a rough vacuum of around $1.0 \cdot 10^{-2}$ torr, which is the pressure needed at the exhaust of the turbo pump which is then turned on and creates a vacuum of around $9.0 \cdot 10^{-8}$ torr. A thermocouple gauge is employed to measure in a pressure range from $7.6 \cdot 10^{2}$ torr to $1.0 \cdot 10^{-3}$ torr. Pressures below this range are measured by a hot-cathode Bayard-Alpert gauge that can measure a vacuum down to $1.0 \cdot 10^{-10}$ torr. The vacuum could be enhanced by baking the entire chamber but this may cause too much contamination on the cleaved Bi_2Se_3 surface. Another option is a cold trap on top of the evaporation chamber extending into the chamber with double walls that can be filled with liquid nitrogen. Each component of the vacuum chamber was attached with a conflat flange that uses oxygen-free copper gaskets and knife-edge flanges. The exception to this is the door

of the chamber that was sealed with a viton O-ring that limits the vacuum to a pressure of about $1.0 \cdot 10^{-8}$ torr.

Once the desired pressure is reached we can proceed with the actual evaporation. A crystal monitor is situated to measure the thickness of the evaporated material. The variac (*VARIable Alternating Current*) is a variable autotransformer that allows us to select an AC output voltage. Another transformer which is in series with the variac and the boat will then decrease the preselected voltage and increase the current, keeping the power the same. Depending on the resistance of the boat, which is mostly affected by its material and its cross section, not much current is needed to reach the melting point of Pb. Typically, I used about 40-50 A rms current to evaporate Pb. In practice, I found that the pressure will increase before the actual evaporation of lead starts. This is due to local heating that leads to more outgassing, and also due to the contamination layers on top of the lead that are coming off. It is therefore important to keep the shutter that blocks the pathway from the boat to the sample closed until we get a steady reading from the crystal monitor and a steady vacuum to keep the sample surface free from unwanted contaminants.

The crystal monitor had to be calibrated since its position is a little bit higher than the sample and is also partially blocked by the sample holder. The determined tooling factor is around 3.0, by which the monitor reading is multiplied to get the total deposition height and deposition rate. Once the crystal monitor gives a steady reading, the shutter is manually opened exposing the sample to the evaporated lead atoms for a certain period of time. The lead atoms will then condense on the surface and, hopefully, form islands. Although we thought that Pb island formation would be easy, I soon realized that ambient conditions rarely resulted in suitably isolated Pb island. Hence, I explored candidate shadow masks that were commercially available. The mask that worked best was a modified TEM grid that is normally used to support free hanging samples for transmission electron microscopy (TEM). As shown in figure 3.4 and 3.5, it is a common circular TEM grid,

made out of Au or Cu, where one side has been coated with an ultrathin (20 nm) carbon membrane that has a periodic array of holes in it. The company *Quantifoil Micro Tools GmbH* has provided us with several masks. It is possible to change the material of the TEM grid, the material of the membrane, the thickness of the membrane, its hole-to-hole distance and the diameter of the holes. It is also possible to create the entire TEM grid and membrane out of SiO_2 which could reduce contamination of the sample surface. The formation of islands and the use of shadow masks is discussed further in sections 4.3 and 4.4.

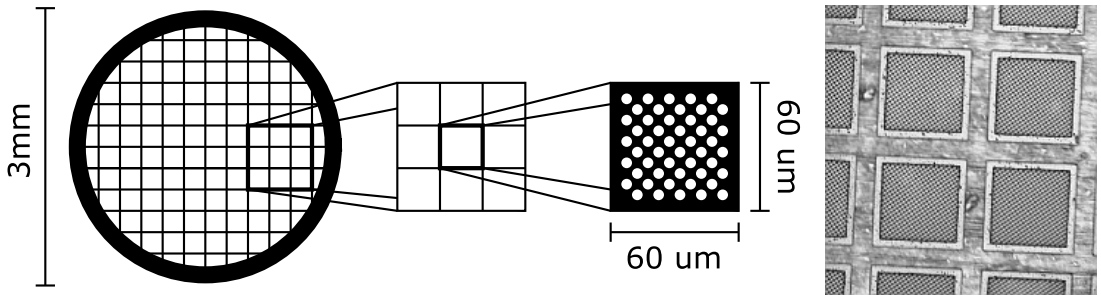

Figure 3.4: Shadow mask. A modified TEM grid served as a shadow mask. Left: The basic circular TEM grid with a diameter of 3 mm is made out of Au. A carbon membrane with circular holes is then placed upon one side of this grid. Right: An optical magnification of the real grid where the carbon membrane with an array of circular holes is visible.

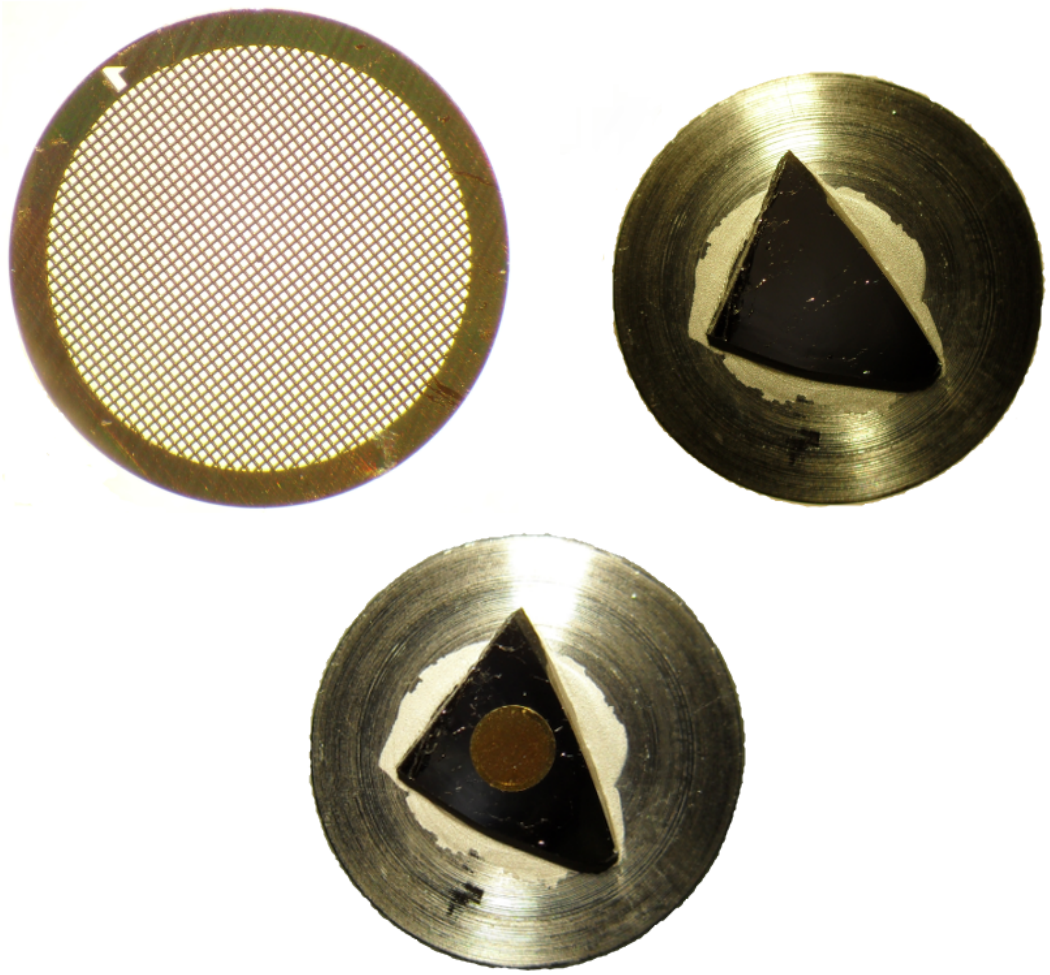

Figure 3.5: Shadow mask and sample. The Au shadow mask with a total diameter of 3 mm is displayed on top (the carbon membrane is not visible in this magnification). The bottom part shows a $Bi_{2.04}Se_3$ crystal that was glued onto a stainless steel STM disk (16 mm diameter) with silver paint. After cleaving the crystal in nitrogen, the shadow mask can be placed on the surface as seen in the bottom right.

3.4 STM Setup

The cryogenic system was an Oxford Heliox^{TL} dewar that was placed on air springs to decouple it from vibrations and served to cool the sample down that was inside the STM scanhead as displayed in figure 3.6 and 3.7. The STM scanhead was attached to the bottom of a long STM stick that can be pushed down inside the Oxford dewar while it is connected to the STM electronics. The dewar has a main bath that can be precooled with liquid nitrogen and then with liquid ^{4}He. The dewar includes a 1 K pot that allows pumping on the ^{4}He to further reduce the temperature. The main bath encases the actual sample space where the STM stick is pushed into and is shielded from the outside by an outer vacuum chamber with superinsulation and an inner vacuum chamber to minimize the boil off of the dewar. The sample space contains a sorption pump and radiation shielding. The inner vacuum chamber can be filled with s small amount (10^{-2} torr) helium exchange gas to enhance the thermal coupling of the sample to the liquid nitrogen or helium bath. Nevertheless, the cooling down procedure takes several hours to ensure that no components, such as the piezo tubes, are thermally shocked and to avoid thermal drift. All spaces should be evacuated in a careful procedure to around 10^{-7} torr before they can be used. The STM itself uses a Besocke type design, i.e. three piezo tubes in a circular arrangement support a sample disk with ramps that is directly placed on top of these piezo tubes that also make an electrical contact directly to the sample. Another piezo tube, in the middle of this arrangement supports the actual STM tip that was mechanically cut from a $Pt_{0.8}Ir_{0.2}$ wire with a diameter of 0.25 mm. This setup allows us to control the tip and the sample in all spatial directions. After cutting, the $Pt_{0.8}Ir_{0.2}$ wire together with a thin gold wire, is glued on a flat Si chip with silver paint or epoxy. The Si chip is then attached to the supporting piezo tube with a small layer of vacuum grease as an adhesive that will freeze at low temperatures. The gold wire is soldered to another fixed wire in the STM scanning head that leads to the external

electronics rack. Now the tip and the sample holder are both electrically connected and a tunneling voltage can be applied. The STM control electronics such as the approach control and the feedback control was purchased from RHK Technology. A separate lock-in amplifier can be included in this circuit to enhance the signal-to-noise ratio.

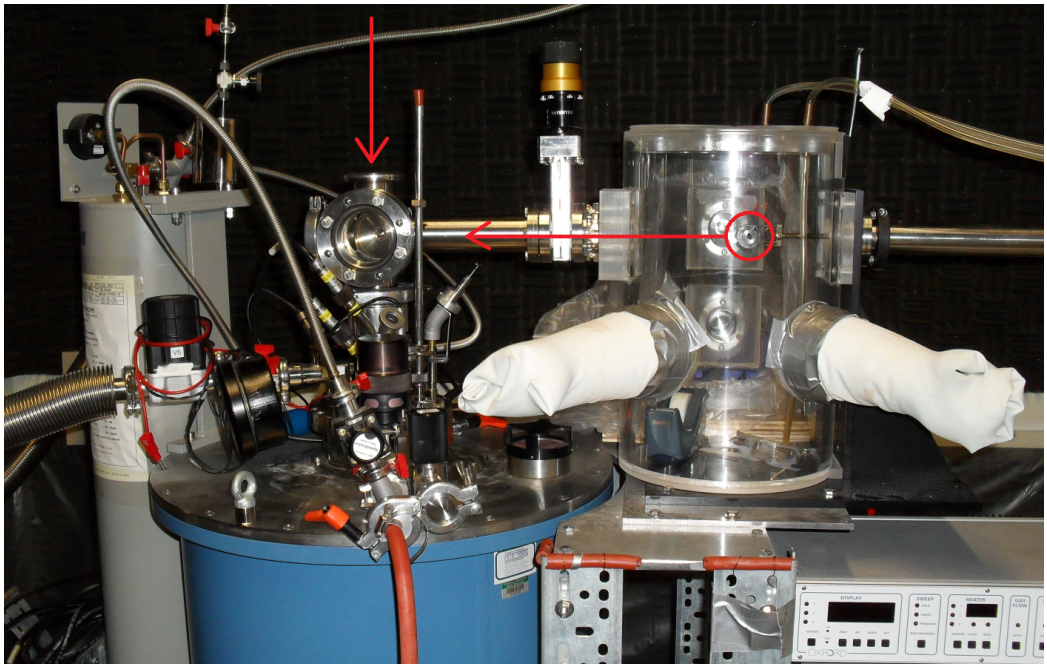

Figure 3.6: STM setup. The blue Oxford Heliox^{TL} dewar is seen in the bottom. The STM scanhead, that contains the STM tip and sample, is pushed inside this dewar (the vertical red arrow shows the entry port and direction of the push down). The scanhead is not in this picture, but is shown in Figure 3.7. The nitrogen filled loading chamber is on the right and contains the processed sample (red circle). A horizontal manipulator can transfer this sample into the STM scanhead.

Figure 3.7: STM scanhead, that contains the STM tip and the sample (sample is not placed on the three outer piezo tube in this picture), and will be pushed down into the blue dewar displayed in Figure 3.6. The four piezo tubes of the Besocke design are visible. The STM tip is glued on a Si chip and is positioned on the inner piezo tube in the middle. The magnetic manipulator, displayed in Figure 3.6, will gently place the sample on top of the outer three piezo tubes.

Chapter 4

Experimental Results

4.1 STM and STS of $Bi_{2.04}Se_3$

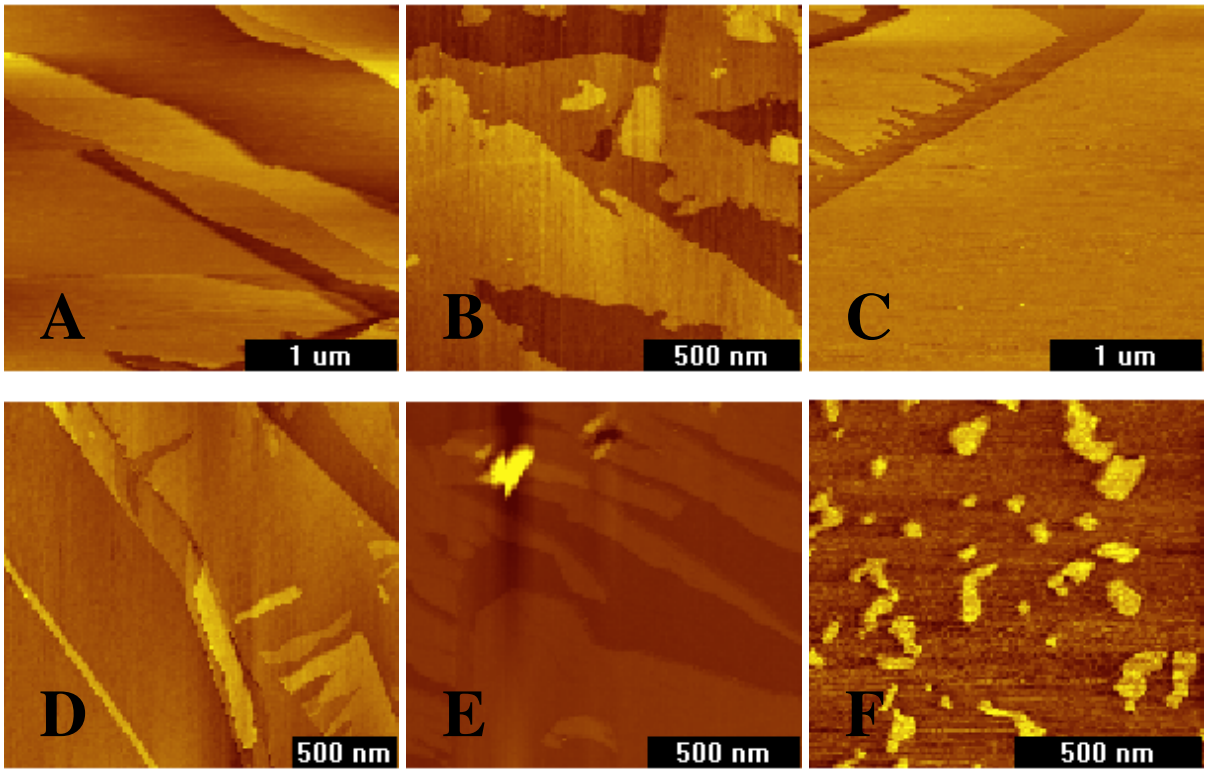

Figure 4.1: **A**, **B**, **C** and **D** show the typical STM topography of $Bi_{2.04}Se_3$ with regions that have a high density of characteristic terraces (z $\sim$ 1 nm) consistent with the expected Bi_2Se_3 quintuple-layer step edges. **E** shows a common tall (z $\sim$ 20 nm) feature that could be due to contamination. **F** shows a cleaving artefact that left island-shaped terraces behind, these can be easily mistaken for self-assembled Pb or Nb islands. Bias voltage was 0.1 V and the current set point 0.1 nA.

The constant current STM topography of $Bi_{2.04}Se_3$ at room temperature gave consistently

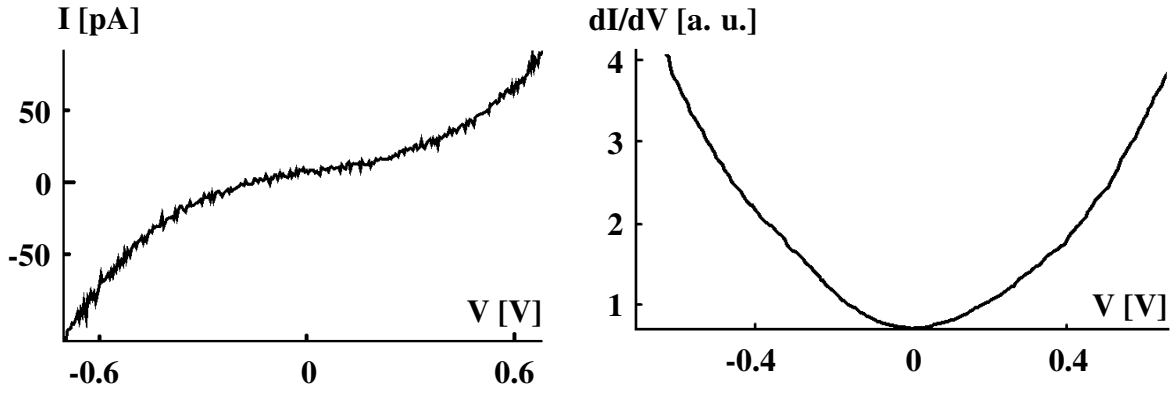

Figure 4.2: Average of 30 I/V and dI/dV curves, taken at one point on the surface of $Bi_{2.04}Se_3$, cleaved in nitrogen and taken at room temperature. The I/V curve has no zero slope and the minimum of the dI/dV curve does not go down to zero but does resemble the characteristic shape of a free 2D electron gas that could have formed on the surface of the probed crystal.

good images where the correct height of 1 nm for the typical terraces, that are shown in figure 4.1, was observed. These terraces typically form after cleaving and sometimes leave cleaving artifacts behind as shown in E and F in figure 4.1, where the tall feature E is probably a contaminant. The typical small islands in F made it sometimes hard to distinguish between these cleaving artefacts and self-assembled Pb or Nb islands after investigating the sample with STM or AFM. The obtained I/V and dI/dV curves as displayed in figure 4.2 were taken at room temperature. One could argue that the non-zero slope of the I/V curve and the non-zero density of states are a sign for surface states or coexisting bulk states extending into the gap, similar to 4.3. But in this case, the data really only shows hints of such features and these curves are probably just a good characterization of a free 2D electron gas on the surface of the crystal.

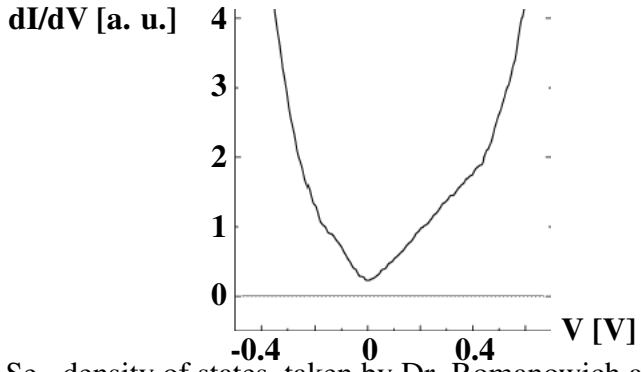

Figure 4.3: $Bi_{2.04}Se_3$ density of states, taken by Dr. Romanowich at 4.2 K. A linear behaviour is seen in the range from -0.2 V to 0.4 V.

4.2 ARPES

ARPES measurements showed that it is very important to consider the environment in which Bi_2Se_3 is measured [3]. The Dirac point is normally around -0.1 eV, only due to outside contamination does it shift to -0.3 eV, where most groups have measured the position of the Dirac point. Since we have cleaved Bi_2Se_3 in nitrogen and keep it in a vacuum of less than $1.0 \cdot 10^{-6}$ torr, we expect to see some effects due to doping and contamination. Dr. Hadj M. Benia from the Max-Planck Institute in Stuttgart was friendly enough to provide us with additional measurements of Bi_2Se_3 that was cleaved in high vacuum (10^{-7} torr) and then exposed to 1 atm nitrogen gas. His measurements show a drastic n-type shift of the Dirac point from -0.1 to -0.4 eV when exposed to Nitrogen. This is believed to be due to induced Se-vacancies. We have recently started collaboration with Dr. Utpal Chatterjee from University of Virginia, who will measure our $Bi_{2.04}Se_3$ sample in order to further test our belief that the Dirac point is indeed at zero as it was shown in figure 4.3

4.3 Nb Sputtering

To prepare a suitable sample, the first approach was to create self-assembled Nb islands on the surface of Bi_2Se_3. Nb is an s-wave superconductor with a very high superconducting transition temperature of 9.3 K. We first sputtered thin Nb films ranging from 10 nm to 50 nm. The result was a complete continuous Nb film that had an increasing surface roughness and grain size with increasing film thickness, typical for sputtered Nb. These observations agreed with results from other STM groups that characterized sputtered Nb films and found that the surface roughness (rms value) is already 1 nm for a 10 nm thick film and over 2 nm for 100 nm thickness whereas the grain size also increases with thickness. [20]. This result was certainly interesting but useless in

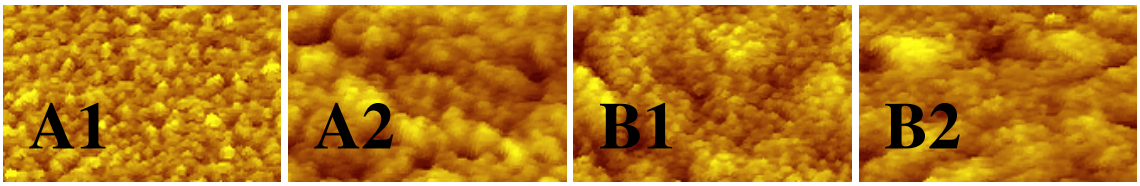

Figure 4.4: STM topography of Nb thin films that were sputtered on Bi_2Se_3. A1 and A2 show the surface of a 10 nm thin film and B1 and B2 show the surface of a 50 nm thin film. A1 and B1 show a 160 nm x 100 nm fragment whereas A2 and B2 show a 30 nm x 20 nm fragment of the surface.

terms of probing the proximity effect where we need seperated superconducting Nb islands on the surface of Bi_2Se_3. We then tried to find the threshold value of the film thickness where separated Nb islands or clusters began to form a continuous surface. Three primary modes of epitaxial thin film growth exist: Volmer-Weber, Frank-van der Merwe and Stranski-Krastanov growth. Since we want to have a clean Bi_2Se_3 surface in between the Nb islands, we do not want a wetting layer or layer-by-layer growth. Island formation without a wetting layer is the Volmer-Weber growth mode. A reasonable thickness to investigate was in the range from 1 nm to 5 nm. Unfortunately we were not able to find this threshold value even with changing the parameters that were described in the previous chapter, such as the Nb target voltage, to decrease the kinetic energy of the arriving Nb

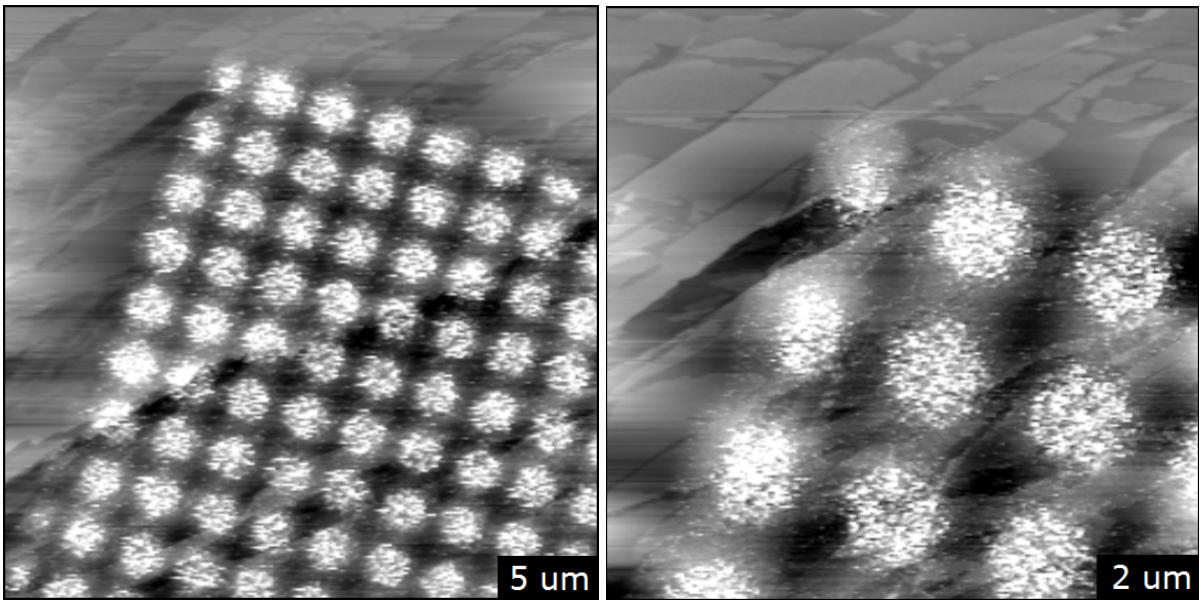

Figure 4.5: AFM topography of a 15 nm thick Nb film that was sputtered on Bi_2Se_3 with a shadow mask. The sputter parameters were: $\mathbf{P} = 2.5 \cdot 10^{-3}$ torr, $\mathbf{U_T}$ = 600 V and $\mathbf{I_P}$ = 0.6 A. The deposition rate was 4.6 Å/s.

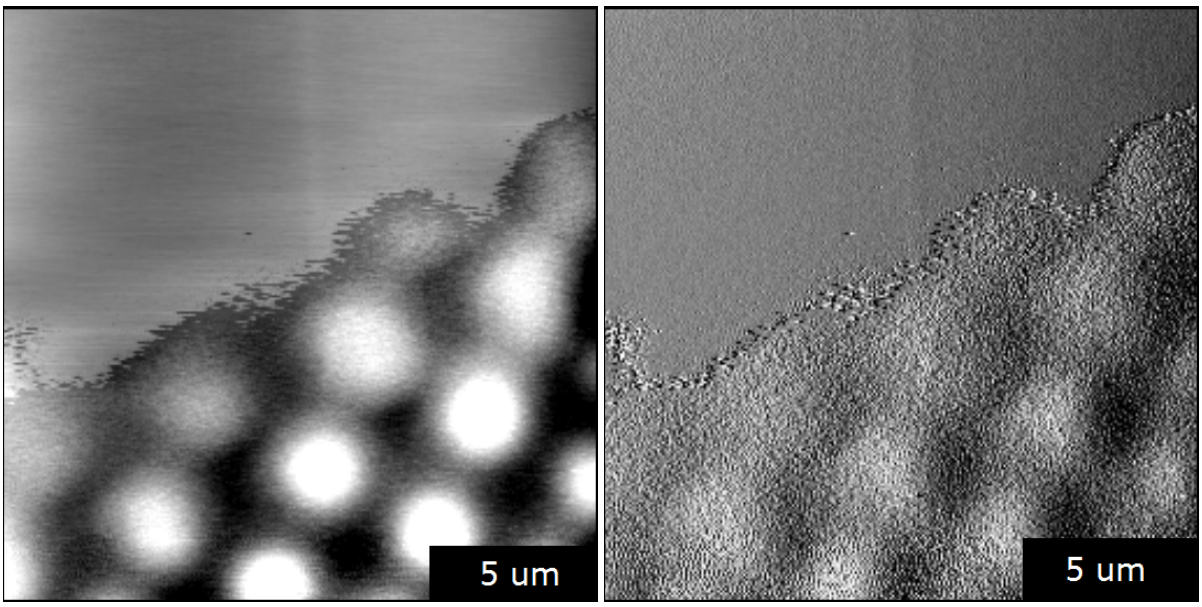

Figure 4.6: AFM topography of a 10 nm thick Nb film that was sputtered on Bi_2Se_3 with a shadow mask. The sputter parameters were: $\mathbf{P} = 1.2 \cdot 10^{-4}$ torr, $\mathbf{U_T}$ = 150 V and $\mathbf{I_P}$ = 0.9 A. The deposition rate was 0.9 Å/s

atoms on the surface or the Ar gas pressure to reduce scattering. The surface was either completely bare or covered with a continuous layer of Nb.

After this approach failed we decided to use a shadow mask to force a controlled island growth. The sputtering parameters were adjusted to get a better step edge coverage but, unfortunately, no choice of parameters led to a satisfactory step edge coverage without shadow effects. An important parameter was the Ar gas pressure that could not be lower than $1.0 \cdot 10^{-4}$ torr for the triode gun to function. $1.0 \cdot 10^{-4}$ torr leads to a mean free path of around 50 cm whereas the normal operating pressure $2.5 \cdot 10^{-3}$ torr yields a mean free path of around 10 cm. Since the distance from the Nb target to the sample surface is around 12 cm and the Nb atoms are also scattering from the walls of the chamber, both values will lead to scattering events that will result in shadow effects. Figure 4.5 shows the topography of a 15 nm thick Nb film that was sputtered through a shadow mask with the normal sputter parameters as listed in the caption. Shadow effects led to diffusion of Nb underneath the mask and did not give us a sharp step edge. Figure 4.6 shows the same procedure but this time for a 10 nm thin Nb film with changed parameters that had the goal to minimize shadow effects. The right image in figure 4.6 displays the amplitude retrace information that directly gives the change in frequency and a better notion of the real topography. The Ar gas pressure was minimized to $1.0 \cdot 10^{-4}$ torr and the Nb target voltage was reduced to 150 V, so that the arriving Nb atoms would not transfer a high kinetic energy in terms of an increased hopping parameter on the sample surface. These parameters led to a better quality of the Nb film; unfortunately, they changed nothing in terms of the shadow effects that still obscured a sharp step edge between the Nb islands and the Bi_2Se_3. Another negative side effect was the constant contamination of the Bi_2Se_3 surface as seen with STM topography in figure 4.7.

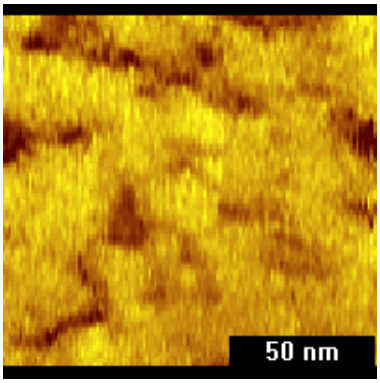

Figure 4.7: Typical STM topography of the surface of Bi_2Se_3 after it was exposed to sputtering. With or without a shadow mask, sample contamination is visible as a very rough topography of the surface, i.e. the black trenches.

4.4 Pb/PbBi Evaporation

We eventually decided to switch to another s-wave superconductor. Pb is a good choice because it has a reasonable high superconducting transition temperature of 7.2 K (bulk value), a low melting point of around 328 $^{\circ}$C and a coherence length of 83 nm. Recent STM experiments suggest that even epitaxial grown Pb islands on Si with a thickness of just a few monolayers already exhibit a superconducting gap [25] [22] [31]. Again, we tried to get self-assembled islands first, since Pb has a natural tendency to form hillocks. Our measurements showed that the distance between separate self-assembled Pb islands, even for a smaller film thickness, is never greater than around 70 nm (as shown in figure 4.8), and is therefore not suitable for probing the proximity effect over a longer length scale that is at least more than twice as long as the coherence length. Since our evaporation chamber, that was assembled specifically for this experiment, provides a reasonable good vacuum of up to $8.0 \cdot 10^{-8}$ torr, the mean free path of the evaporated Pb atoms is over 1000 m and thus will significantly reduce shadow effects allowing us to try a shadow mask once again.

Figures 4.9, 4.10 and 4.11 show Pb islands that were evaporated through a shadow mask in this

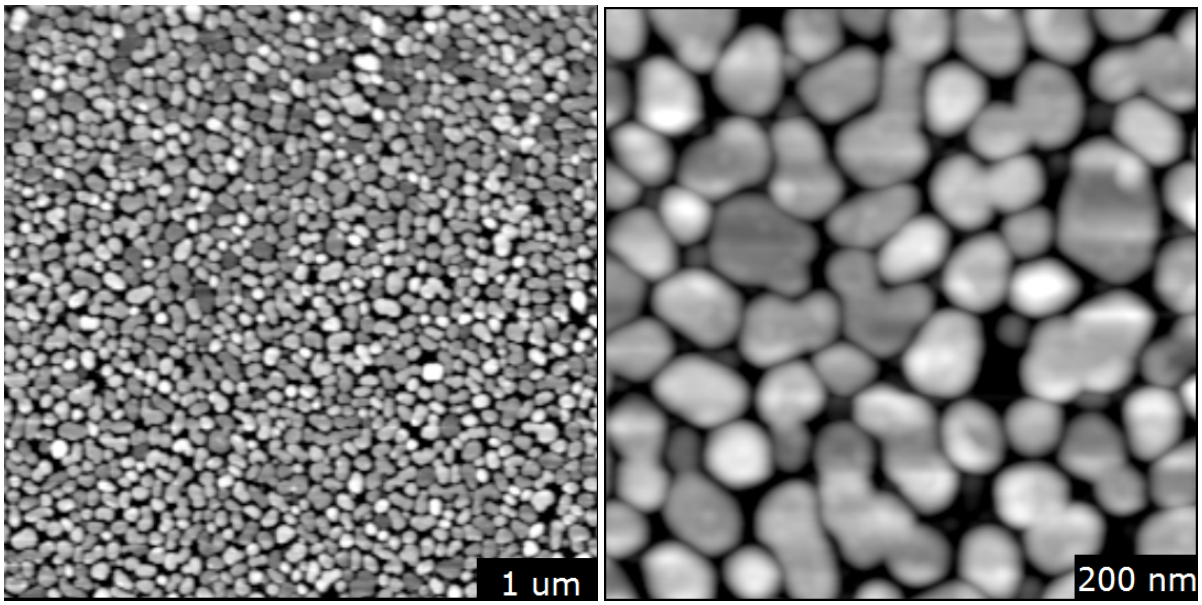

Figure 4.8: A thin Pb film (20 nm) was evaporated on the surface of Bi_2Se_3. Typical hillock formation was observed. The pressure during evaporation was $\mathbf{P} = 5 \cdot 10^{-5}$ torr, the current $\mathbf{I} = 78$ A and the evaporation rate 2.0 Å/s. These values are from the evaporation chamber in the advanced laboratory that was used as a first test to investigate Pb on Bi_2Se_3.

desired pressure range. The Pb islands have a well defined and sharp edge that separates the clean $Bi_{2.04}Se_3$ surface from the Pb island. Since Pb naturally has a tendency to form hillocks on almost any material, the Pb islands were not continuous but consisted of smaller islands themselves. Figure 4.11 outlines a bigger hillock right at the edge that would be suitable for probing the proximity effect at precisely this position. Since Pb has this intrinsic tendency to form hillocks and also undergoes a lattice change when cooled down, we decided to also investigate PbBi alloys that basically help to create a more continuous film. Depending on the ratio of Pb to Bi, the superconducting transition temperature can be enhanced up to 9.3 K [24]. Figure 4.12 shows the topography of a 20 nm thin PbBi film that was evaporated on $Bi_{2.04}Se_3$ through a shadow mask. This was done in the inferior evaporation chamber in the advanced laboratory that only provides a vacuum up to $5.0 \cdot 10^{-5}$ torr, and thus, shadow effects are leading to contamination of the $Bi_{2.04}Se_3$ surface between the PbBi islands. This can be avoided in the optimized evaporation chamber that

provides a better vacuum.

The optimized evaporation chamber produced reproducible results with no shadow effects or observable contamination of the $Bi_{2.04}Se_3$ surface, which does not mean that there is no actual contamination. Beside the low vacuum, the carbon membrane shadow mask, that was pushed against the $Bi_{2.04}Se_3$ surface, helped to reduce shadow effects with a thickness of only 20 nm.

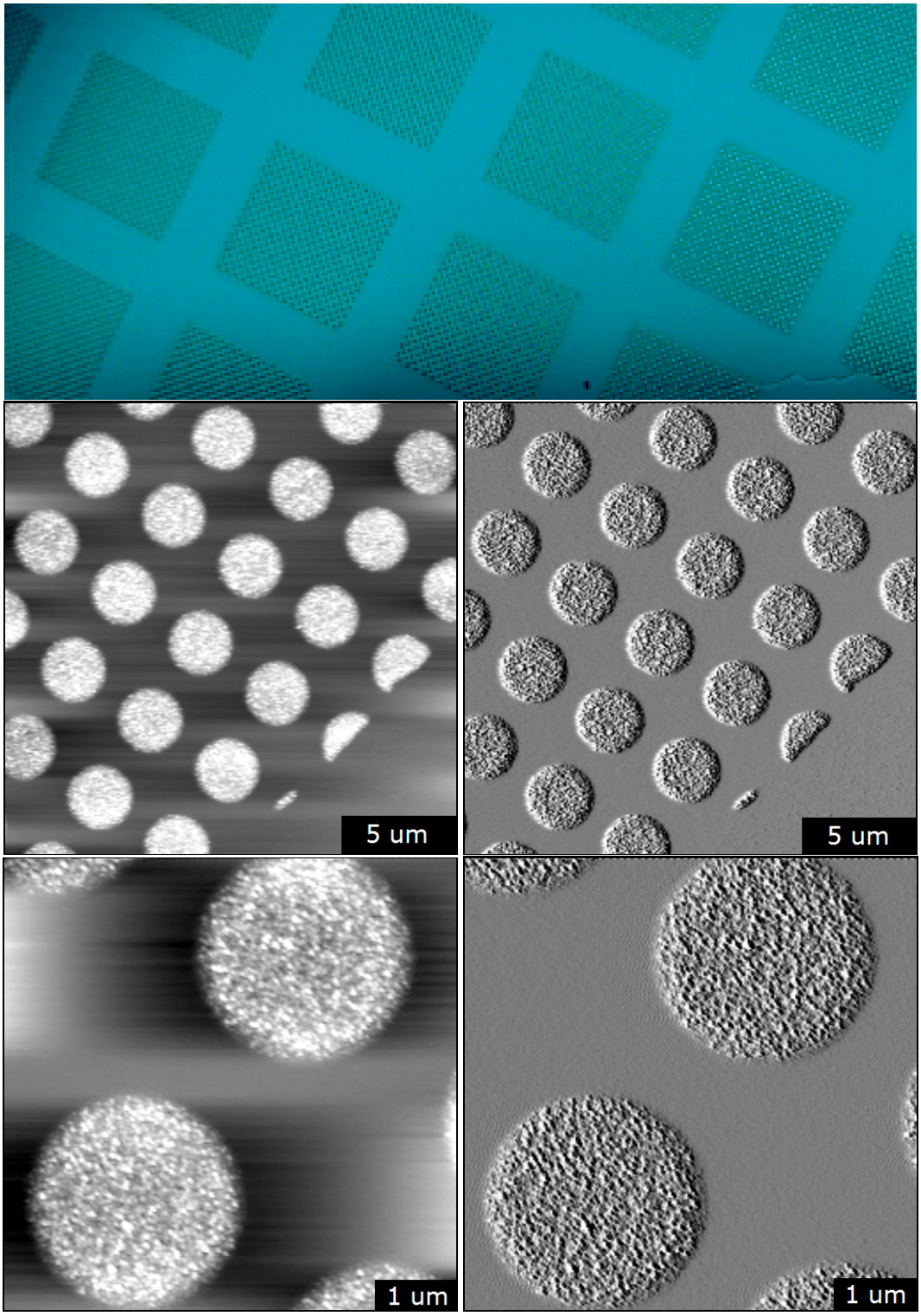

Figure 4.9: AFM topography of a 12 nm thin Pb film, evaporated on $Bi_{2.04}Se_3$ through a shadow mask. An optical magnification of the sample surface on top shows the typical arrangment of the islands due the the geometry of the shadow mask as outlined in figure 3.4. The pressure during evaporation was **P** = $9.2 \cdot 10^{-8}$ torr, the current **I** = 49 A and the evaporation rate 0.5 Å/s (* 3 = 1.5 Å/s due to conversion factor).

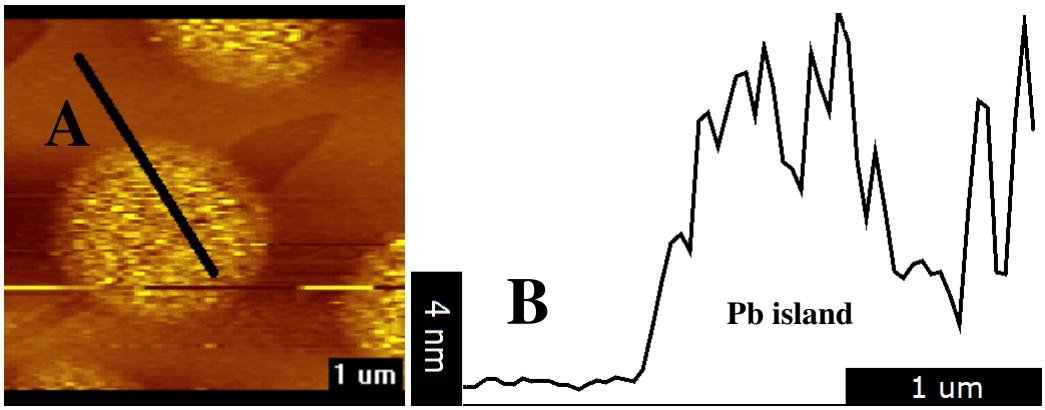

Figure 4.10: STM topography of evaporated Pb islands that were created by using a shadow mask. The height profile of the black line in A is displayed in B and shows the typical surface roughness of one Pb island. The dip might be due to the terrace that is visible in A underneath the Pb island.

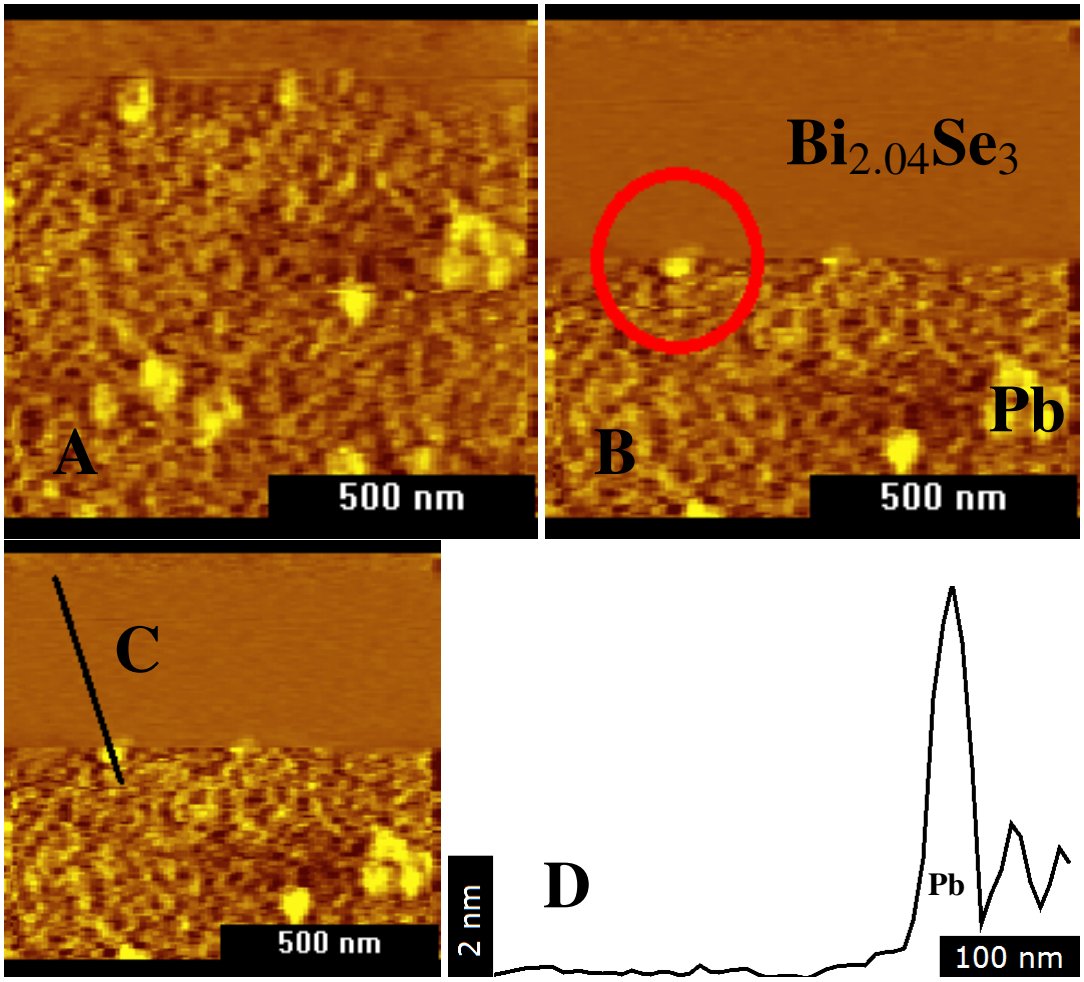

Figure 4.11: A shows the STM topography of a Pb island, the typical tendency of Pb to form hillocks is clearly observed. A larger hillock at the edge of the island is picked out in B. The height profile in C and D show a sharp edge along this hillock that could be suitable for probing the proximity effect.

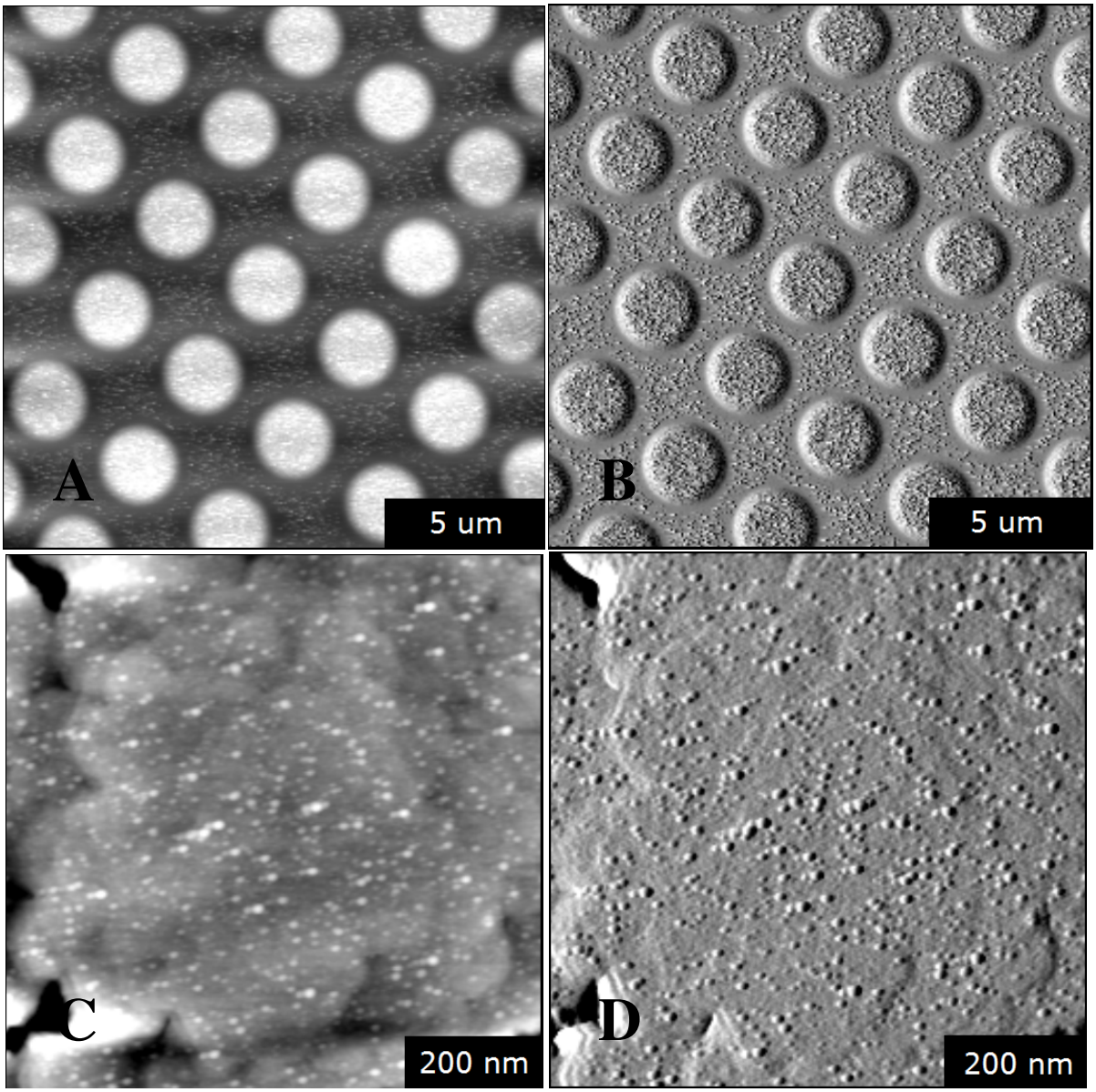

Figure 4.12: AFM topography of a 20 nm thin PbBi film, evaporated on $Bi_{2.04}Se_3$ through a shadow mask. A and B show more continuous islands but also shadow effects due to the low vacuum and higher evaporation rate in the advanced laboratory evaporation chamber. The halo around each island is probably due to a diffusion of nearby atoms into the bigger island. The focus in C and D is directly on top of the PbBi island that has a more continuous surface and less hillocks as Pb would have created. The pressure during evaporation was $\mathbf{P} = 8.8 \cdot 10^{-5}$ torr, the current **I** = 76 A and the evaporation rate 2.6 Å/s. These values are from the evaporation chamber in the advanced lab.

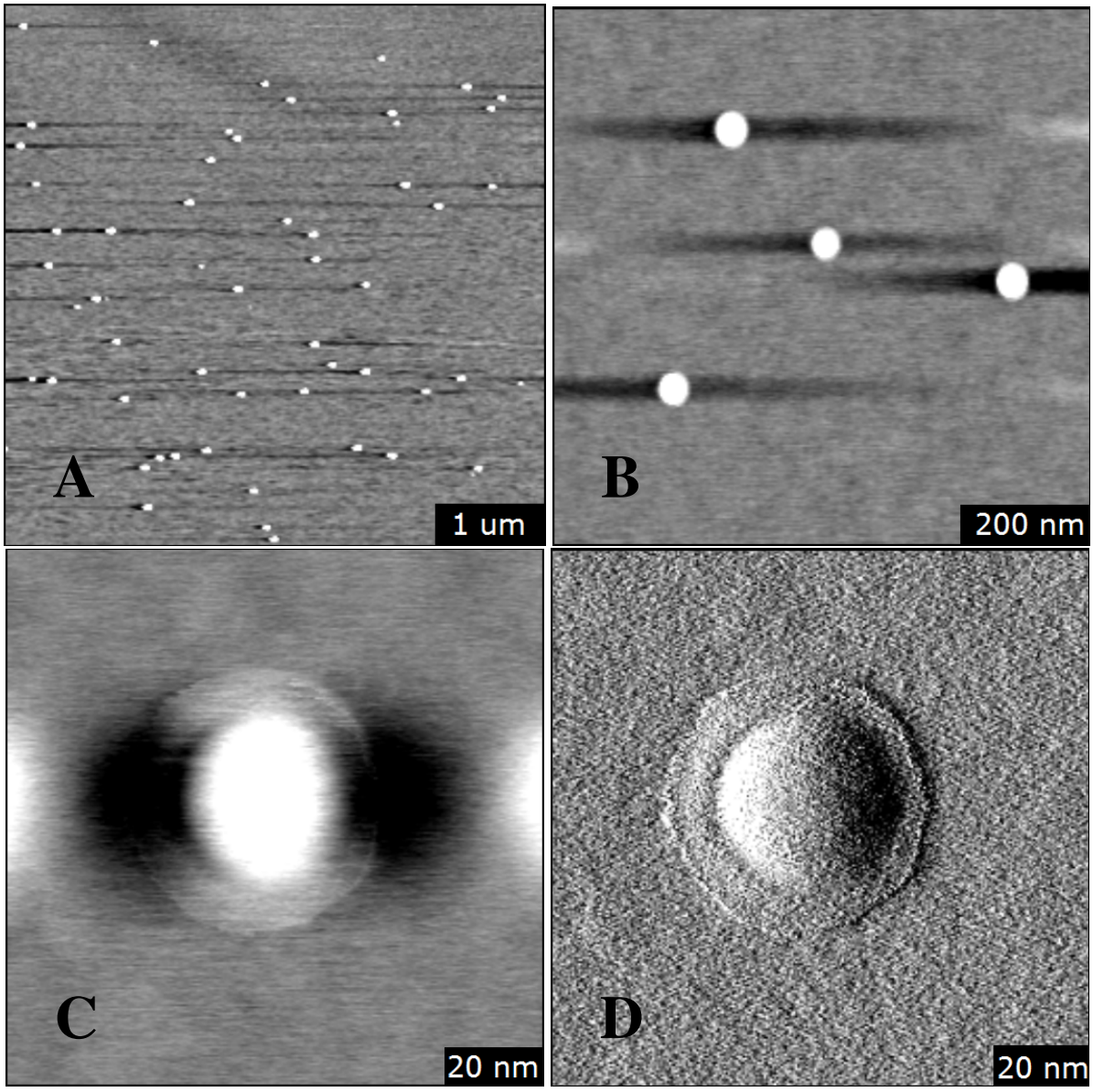

Figure 4.13: **A** and **B**: AFM topography of typical but unknown contaminants (z $\sim$ 2 nm) on $Bi_{2.04}Se_3$ after leaving it in a polystyrene petri dish. Probably non-conducting since these contaminants were never observed with STM. The *egg-like* shape of a single contaminant in **C** is enhanced by just displaying the amplitude retrace information content in **D**.

Chapter 5

Discussion

5.1 Position of the Dirac cone

Bi_2Se_3 is n-type due to Se vacancies and the Dirac point in clean samples typically resides between 0 and -0.3 eV, depending on the cleaving environment as shown in the ARPES section. A first motivation to get excess bismuth doped samples was to probe defects. Now, Bi doping would actually make it even more n-type. We can therefore ask the legitimate question why we measured a linear density of states near zero energy in the first place, as it has been done in a careful experiment by Dr. Romanowich on our $Bi_{2.04}Se_3$ samples, executed last year [29] and shown in figure 4.3.

The spectroscopy showed a linear density of states in the range of the approximate bandgap of 0.3 eV with the minimum being at 0 eV. This is intriguing because it is not consistent with previous measurements on Bi_2Se_3 that were done by Dr. Urazhdin, who found, in accordance with other groups, that the Dirac point resides at -0.3 eV for Bi_2Se_3 [35]. When we re-investigated the exact same Bi_2Se_3 samples, the minimum in the density of states showed up around 0 V, just like for our new sample $Bi_{2.04}Se_3$. However, the shape of the curve is exactly the same for Dr. Urazhdin and Dr. Romanwoich measurements, which is strong evidence for the same underlying physics. I believe, the difference between the two measurements was, that Dr. Urazhdin cleaved in helium gas while we now cleave in nitrogen gas that might dope the sample surface in a different way. He also did not use silver paint to glue the sample to the STM disk. Silver paint is known for

outgassing in vacuum and it could also dope the sample unintentionally.

The unit cell analysis of our crystal growth collaborators showed that the lattice expanded due to the excess bismuth. One can speculate that this effect made the samples more stable against external influences such as doping, since recent ARPES measurements showed that the native position of the Dirac point is actually closer to zero energy than previously thought [3]. Pure STS measurements do not directly measure the dispersion relation Energy **E** vs. momentum **k**.

Combining our STS measurements with other methods that can verify the position of the Dirac point would be a good way to support and complement our data. One way to achieve this in our STM system is, to turn on the magnetic field inside the dewar and count the Landau levels which will show where the bulk bands and the Dirac point are. This has been done before by a STM group that found the zeroth Landau level that is predicted to give rise to the half-quantized Hall effect for the topological surface states [8]. Another STM technique is to perform FT-STM, that will fourier transform from real space into momentum space and basically show us the Brillouin zone. We also hope to get supporting results from our new ARPES collaboration, that is currently investigating our Bi_2Se_3 and $Bi_{2.04}Se_3$ samples mentioned in the previous chapter.

5.2 Pro et contra of different deposition methods and suggested improvements

The main objective was to produce superconducting structures on top of a $Bi_{2.04}Se_3$ surface without contaminating this surface. Discussions with other faculty members gave several ideas how to accomplish this:

- Photolithography
- Nanosphere lithography
- Alloy phase separation, where the non-superconducting material is etched away
- Self-assembly
- Shadow mask
- Angle shadowing to produce trenches
- Deposit Nb-nanoparticles on the surface and heat the sample to create an interface.
- Second Nb-tip that is crashed into, or brought close to the surface, while the other STM tip is investigating the proximity effect

From these ideas, only a few are realistic that won't contaminate the surface of $Bi_{2.04}Se_3$ too much. It is important to stress the fact that we cleaved and processed the cleaved $Bi_{2.04}Se_3$ crystal **ex-situ**, which means that we had to break vacuum after processing in order to transport the sample into the high-vacuum STM for further investigation. Another factor besides contamination is the influence on the STM tip. In 1994, Stroscio already pointed out that for dirty surfaces the current varies less rapidly than expected with vertical displacement of the tip and wrote that this

can be explained by assuming that the dirt on the sample surface mediates a mechanical interaction between surface and tip, i.e. some insulating dirt (e.g. oxide) is squeezed between the surface and tip, acting in effect as a spring [14].

We tried to minimize the sample exposure to air by keeping the sample in a nitrogen environment at all times. Past measurements from Dr. Urazhdin and Dr. Romanwich showed that our STM does indeed produce reproducible results, but under these described circumstances we must be aware of the impact of contaminants when the sample is further processed. Recent breakthroughs in surface science were possible because a complete **in-situ** handling of the sample was possible, which means that an ultra-high vacuum (below 10^{-9} Torr, mostly 10^{-11} to 10^{-12} Torr) had to be maintained throughout the entire preparation, processing and measurement of the sample at all times. Another advantage of an ultra-high vacuum and in-situ handling is the possibility to grow nanostructures epitaxially, because the evaporation rate can be decreased significantly while the UHV ensures that only few contaminants react with the evaporating atoms or contaminate the interface of the substrate and the evaporant during the growth process as it is done for molecular beam epitaxy. Under these conditions it is possible to grow nanostructures on a substrate as has been shown in a recent paper that investigated the superconducting proximity effect from Pb islands into a normal metal with STM [31]. This paper and two other ones that investigated superconductivity in Pb islands showed that Pb islands already become superconducting for a thickness of two or three monolayers and a width that is comparable to the coherence length of Pb (83 nm) [25] [22]. Although these results are only true for epitaxially grown Pb islands, they give us hope that small Pb-islands with a thickness well below the coherence length of 83 nm will still show a stable superconducting gap in STS measurements. We decided that under these conditions smaller islands that are 5-10 nm thick should be sufficient, although in this regime, quantum confinement effects might play an interesting role and lead to bound states within the island.

The experimental results in this thesis showed that we can get the right geometry (i.e the geometry in figure 4.11) to probe the proximity effect. The island geometry is also suitable to probe another effect proposed by Fu and Kane [13] where they propose a superconducting trijunction on a topological insulator, where Majorana modes could be adjusted by controlling the phase of each junction. Another application of the island array is a transport measurement that will measure a current going from one side of the array to the other side where the transport relies on the superconducting proximity effect. For these last two proposals it is better to evaporate PbBi instead of Pb since that will lead to a more continuous island surface. The antidot experiment, as it is proposed in [13], could be realized by growing a continuous PbBi or Nb film on a topological insulator and then ion mill through the shadow mask to create the antidot structure. The reproducible process, that led to the geometries presented in this thesis, was found after some time-consuming experiments. Unfortunately, due to the rather short time clock of my Masters thesis, there was not enough time left to probe the proximity effect at liquid helium temperature. Two approaches in the last few weeks failed because the tip kept crashing during the cool-down procedure. This might be due to the inexperience of the user or due to the tall Pb hillocks that might have an oxide layer and cause the STM tip to crash. This is still under current investigation and I am confident that there is a good chance to probe the proximity effect within the next few months.

Regarding future measurements, I propose some adjustments to this experiment that would make a measurement easier in the future. The evaporation chamber should be directly connected to the STM to make an in-situ sample preparation possible. One could think about a separate loading chamber that allows to bake the entire STM and evaporation chamber in advance, without contaminating the sample if a UHV environment is desired. One way to achieve UHV would be to directly attach an ion-pump to the STM chamber. An ion-pump has no moving parts and achieves UHV by accelerating electrons across a volume that will ionize remaining molecules within this

volume which will then stick to chemically reactive plates on the walls of the pump. Regarding the contamination from the shadow mask and sample holder, a simple solution would be to separate the shadow mask from the crystal surface and order a shadow mask that is completely made out of Au or SiO_2 without any carbon or plastic residues as it was already offered by the company that fabricates this mask. One way to separate the shadow mask from the sample surface is to bring it in close proximity to the sample surface inside the evaporation chamber (only a few microns away to reduce shadow effects) by controlling the approach with an optical microscope.

Since discussions with other STM groups gave the insight that Pb does not grow epitaxially on Bi_2Se_3, regardless of growth temperature, it would be wise to try Nb again. I would not recommend sputtering since this would require an ex-situ handling and introduce other factors such as Ar doping and unknown contaminants from the sputtering chamber. Instead, an e-beam evaporator, directly attached to the STM chamber, might be a good solution to control Nb island growth.

BIBLIOGRAPHY

BIBLIOGRAPHY

[1] Colin Conrad Adams and Robert David Franzosa. *Introduction to topology: pure and applied*. Pearson Prentice Hall, Upper Saddle River, NJ, 2008.

[2] J. E. Avron, R. Seiler, and B. Simon. Homotopy and quantization in condensed matter physics. *Physical Review Letters*, 51(1):51–53, July 1983.

[3] Hadj M. Benia, Chengtian Lin, Klaus Kern, and Christian R. Ast. Reactive chemical doping of the bi_{2}se_{3} topological insulator. *Physical Review Letters*, 107(17):177602, October 2011.

[4] B. Andrei Bernevig. *Topological insulators and topological superconductors*. Princeton University Press, Princeton, N.J.; Woodstock, 2013.

[5] M. V. Berry. Quantal phase factors accompanying adiabatic changes. *Proceedings of the Royal Society of London. A. Mathematical and Physical Sciences*, 392(1802):45–57, August 1984.

[6] Michael Berry. Anticipations of the geometric phase. *Physics Today*, 43(12):34–40, 1990.

[7] Annica M. Black-Schaffer and Alexander V. Balatsky. Proximity-induced unconventional superconductivity in topological insulators. arXiv e-print 1305.4142, May 2013. Phys. Rev. B 87, 220506(R) (2013).

[8] Peng Cheng, Canli Song, Tong Zhang, Yanyi Zhang, Yilin Wang, Jin-Feng Jia, Jing Wang, Yayu Wang, Bang-Fen Zhu, Xi Chen, Xucun Ma, Ke He, Lili Wang, Xi Dai, Zhong Fang, Xincheng Xie, Xiao-Liang Qi, Chao-Xing Liu, Shou-Cheng Zhang, and Qi-Kun Xue. Landau quantization of topological surface states in bi_{2}se_{3}. *Physical Review Letters*, 105(7):076801, August 2010.

[9] Herv Courtois, Philippe Gandit, Bernard Pannetier, and Dominique Mailly. Long-range coherence and mesoscopic transport in NS metallic structures. *Superlattices and Microstructures*, 25(56):721–732, May 1999.

[10] Liang Fu and C. L. Kane. Time reversal polarization and a z_2 adiabatic spin pump. arXiv e-print cond-mat/0606336, June 2006. Phys. Rev. B 74, 195312 (2006).

[11] Liang Fu and C. L. Kane. Superconducting proximity effect and majorana fermions at the surface of a topological insulator. arXiv e-print 0707.1692, July 2007. Phys. Rev. Lett. 100, 096407 (2008).

[12] Liang Fu and C. L. Kane. Topological insulators with inversion symmetry. *Physical Review B*, 76(4):045302, July 2007.

[13] M. Z. Hasan and C. L. Kane. Topological insulators. arXiv e-print 1002.3895, February 2010. Rev.Mod.Phys.82:3045,2010.

[14] William Joseph Kaiser. *Scanning tunneling microscopy*. Acad. Press, San Diego [u.a., 1994.

[15] C. L. Kane and E. J. Mele. Z_2 topological order and the quantum spin hall effect. arXiv e-print cond-mat/0506581, June 2005. Phys. Rev. Lett. 95, 146802 (2005).

[16] A. Yu Kitaev. Unpaired majorana fermions in quantum wires. *Physics-Uspekhi*, 44(10S):131, October 2001.

[17] K. v. Klitzing, G. Dorda, and M. Pepper. New method for high-accuracy determination of the fine-structure constant based on quantized hall resistance. *Physical Review Letters*, 45(6):494–497, August 1980.

[18] Mahito Kohmoto. Topological invariant and the quantization of the hall conductance. *Annals of Physics*, 160(2):343–354, April 1985.

[19] Gad Koren, Tal Kirzhner, Yoav Kalcheim, and Oded Millo. Signature of proximity induced triplet superconductivity in junctions made of the doped topological insulator $\rm Bi_2Se_3$ and the s-wave superconductor NbN. arXiv e-print 1303.0652, March 2013.

[20] V. Lacquaniti, S. Maggi, E. Monticone, and G. B. Picotto. Surface characterization of sputtered niobium films by scanning tunneling microscopy. In *The 1993 international conference on scanning tunneling microscopy*, volume 12, pages 1734–1737, Beijing, China, 1994. AVS.

[21] R. B. Laughlin. Quantized hall conductivity in two dimensions. *Physical Review B*, 23(10):5632–5633, May 1981.

[22] Jiepeng Liu, Xuefeng Wu, Fangfei Ming, Xieqiu Zhang, Kedong Wang, Bing Wang, and Xudong Xiao. Size-dependent superconducting state of individual nanosized pb islands

grown on si(111) by tunneling spectroscopy. *Journal of Physics: Condensed Matter*, 23(26):265007, July 2011.

[23] V. Mourik, K. Zuo, S. M. Frolov, S. R. Plissard, E. P. a. M. Bakkers, and L. P. Kouwenhoven. Signatures of majorana fermions in hybrid superconductor-semiconductor nanowire devices. *Science*, 336(6084):1003–1007, May 2012. PMID: 22499805.

[24] James E. Nicholson and Kerry G. Coffman. Trends of superconducting transition temperatures in ternary alloys of lead, bismuth, and group 3A elements. *Journal of Low Temperature Physics*, 45(5-6):429–441, December 1981.

[25] Takahiro Nishio, Masanori Ono, Toyoaki Eguchi, Hideaki Sakata, and Yukio Hasegawa. Superconductivity of nanometer-size pb islands studied by low-temperature scanning tunneling microscopy. *Applied Physics Letters*, 88(11):113115–113115–3, March 2006.

[26] Xiao-Liang Qi and Shou-Cheng Zhang. The quantum spin hall effect and topological insulators. *Physics Today*, 63(1):33–38, 2010.

[27] Xiao-Liang Qi and Shou-Cheng Zhang. Topological insulators and superconductors. arXiv e-print 1008.2026, August 2010. Rev. Mod. Phys. 83, 1057-1110 (2011).

[28] Fanming Qu, Fan Yang, Jie Shen, Yue Ding, Jun Chen, Zhongqing Ji, Guangtong Liu, Jie Fan, Xiunian Jing, Changli Yang, and Li Lu. Strong superconducting proximity effect in pb-Bi2Te3 hybrid structures. *Scientific Reports*, 2, March 2012. PMID: 22468226 PMCID: PMC3314303.

[29] Megan Romanowich, Mal-Soon Lee, Duck-Young Chung, Jung-Hwan Song, S. D. Mahanti, Mercouri G. Kanatzidis, and Stuart H. Tessmer. The interplay of topological surface and bulk electronic states in Bi2Se3. arXiv e-print 1210.1874, October 2012.

[30] Satoshi Sasaki, M. Kriener, Kouji Segawa, Keiji Yada, Yukio Tanaka, Masatoshi Sato, and Yoichi Ando. Topological superconductivity in cu_{x}bi_{2}se_{3}. *Physical Review Letters*, 107(21):217001, November 2011.

[31] L. Serrier-Garcia, J. C. Cuevas, T. Cren, C. Brun, V. Cherkez, F. Debontridder, D. Fokin, F. S. Bergeret, and D. Roditchev. Scanning tunneling spectroscopy study of the proximity effect in a disordered two-dimensional metal. *Physical Review Letters*, 110(15):157003, April 2013.

[32] Barry Simon. Holonomy, the quantum adiabatic theorem, and berry's phase. *Physical Review Letters*, 51(24):2167–2170, December 1983.

[33] S. H. Tessmer, M. B. Tarlie, D. J. Van Harlingen, D. L. Maslov, and P. M. Goldbart. Probing the superconducting proximity effect in NbSe_{2} by scanning tunneling microscopy. *Physical Review Letters*, 77(5):924–927, July 1996.

[34] D. J. Thouless, M. Kohmoto, M. P. Nightingale, and M. den Nijs. Quantized hall conductance in a two-dimensional periodic potential. *Physical Review Letters*, 49(6):405–408, August 1982.

[35] S. Urazhdin, D. Bilc, S. H. Tessmer, S. D. Mahanti, Theodora Kyratsi, and M. G. Kanatzidis. Scanning tunneling microscopy of defect states in the semiconductor bi_{2}se_{3}. *Physical Review B*, 66(16):161306, October 2002.

[36] Mei-Xiao Wang, Canhua Liu, Jin-Peng Xu, Fang Yang, Lin Miao, Meng-Yu Yao, C. L. Gao, Chenyi Shen, Xucun Ma, X. Chen, Zhu-An Xu, Ying Liu, Shou-Cheng Zhang, Dong Qian, Jin-Feng Jia, and Qi-Kun Xue. The coexistence of superconductivity and topological order in the Bi2Se3 thin films. *Science*, 336(6077):52–55, June 2012. PMID: 22422860.

[37] E. Wigner. Ueber die operation der zeitumkehr in der quantenmechanik. *Nachrichten von der Gesellschaft der Wissenschaften zu Gttingen, Mathematisch-Physikalische Klasse*, 1932:546–559.

[38] Ai Yamakage, Keiji Yada, Masatoshi Sato, and Yukio Tanaka. Theory of tunneling conductance and surface-state transition in superconducting topological insulators. *Physical Review B*, 85(18):180509, May 2012.

[39] Fan Yang, Yue Ding, Fanming Qu, Jie Shen, Jun Chen, Zhongchao Wei, Zhongqing Ji, Guangtong Liu, Jie Fan, Changli Yang, Tao Xiang, and Li Lu. Proximity effect at superconducting sn-bi_{2}se_{3} interface. *Physical Review B*, 85(10):104508, March 2012.

[40] Parisa Zareapour, Alex Hayat, Shu Yang F. Zhao, Michael Kreshchuk, Achint Jain, Daniel C. Kwok, Nara Lee, Sang-Wook Cheong, Zhijun Xu, Alina Yang, G. D. Gu, Shuang Jia, Robert J. Cava, and Kenneth S. Burch. Proximity-induced high-temperature superconductivity in the topological insulators Bi2Se3 and Bi2Te3. *Nature Communications*, 3:1056, September 2012.

[41] Duming Zhang, Jian Wang, Ashley M. DaSilva, Joon Sue Lee, Humberto R. Gutierrez, Moses H. W. Chan, Jainendra Jain, and Nitin Samarth. Superconducting proximity effect and possible evidence for pearl vortices in a candidate topological insulator. *Physical Review B*, 84(16):165120, October 2011.